Zebrafish xenograft model: Identification of novel mechanisms driving prostate cancer metastasis

Chen, L.

Chapter 4

Enhanced mechanosensing and mechanotransduction potential of prostate cancer stem-like cells promotes metastatic tumor initiation

Lanpeng Chen[1], Marta De Menna[2], Stefano Coppola[3], Nick Landman[1], Sebastiaan Schieven[1], Arwin Groenewoud[1], George N. Thalmann, [2,4] Thomas Schmidt[3], Marianna Kruithof-de Julio[2,4*] and B. Ewa Snaar-Jagalska[1*]

[1]Institute of Biology, Leiden University, Leiden, Netherlands

[2] Department for BioMedical Research, Bern University, Bern, Switzerland

[3] Institute of Physics, Leiden University, Leiden, Netherlands

[4]Department of Urology, Inselspital, Bern , Switzerland

*Corresponding authors

Dr. PD Marianna Kruithof-de Julio, marianna.kruithofdejulio@dbmr.unibe.ch

Prof. B. Ewa Snaar-Jagalska, b.e.snaar-jagalska@biology.leidenuniv.nl

Submitted

Abstract

Analysis of clinical datasets indicate that cancer stem cells (CSCs) derived from prostate cancer (PCa) patients display an elevated expression of genes for cell-matrix interactions, cell adhesion proteins and of the putative mechanotransducer TAZ. Here we combined measurements on the cellular mechano-responses to matrix stiffness, including cell-generated forces, together with zebrafish and mouse xenografts as well as PDX-derived organoid models, to show that the stemness phenotype and its related metastatic tumorigenicity of PCa CSC-like cells are associated to their enhanced mechanosensing and mechanotransduction potential. We show that, at metastatic onset, β1-integrin and its interactor ILK are progressively expressed in CSC-like cells, which leads to cellular mechanoresponse through CDC42-N-Wasp-Cortactin dependent cytoskeletal tension, inducing TAZ translocation to the nucleus. As a result expression of the pluripotency genes NANOG and OCT4 is induced which finally leads to initiation of metastatic tumor outgrowth. We further demonstrate that perturbation of this mechanoresponse cascade inhibits metastasis in zebrafish and mice xenografts, and it disrupts growth of PDX-derived organoids. Our data highlight the essential role of mechanosensing and mechanotransduction in PCa metastasis initiation, thereby underling this pathway as an interesting therapeutic target for future studies.

Introduction

Incurable bone metastasis is a main cause of death in prostate cancer (PCa) [1]. It is suggested to be initiated by cancer stem cells (CSCs) [2-5]. CSCs derived from PCa patients displayed a significantly enhanced expression of gene signatures for various focal adhesion proteins [6]. Hence, the cell adhesion molecules CD44 and integrin α2β1 have been used as PCa CSC markers. Both proteins as indicator of cancer stemness are functionally involved in PCa progression, through the strengthening of focal adhesions, altering cytoskeleton dynamics and built-up of cytoskeletal tension, all implicated in the initiation of metastasis [2, 6, 7].

Focal adhesions transduce external mechanical cues into biochemical signals inside cells inducing cytoskeleton remodeling and dynamics [8, 9]. Numerous proteins are involved in this regulation including integrins, focal-adhesion kinases (FAKs), various small-GTPases, Wasp family proteins, DIAPHs and MLCs [9]. When integrins bind to the extracellular matrix (ECM) during cell adhesion and cells are stimulated mechanically, FAKs are phosphorylated and activate the small-GTPases RhoA, RAC1 and/or CDC42. The latter activate downstream signaling cascades that control actin disassembly-reassembly dynamics, which finally lead to the formation of filopodia, stress fibers, lamellipodia and/or invadopodia. Those dynamic actin structures are required for cell migration, cell spreading, and invasion [9-11]. The whole process has been summarized as mechanotransduction, as a transduction of mechanical signals from the microenvironment into cells [12]. One of the signature of mechanotransduction is a modulation of gene expression and metabolisms when cells are

cultured in dishes of varying matrix rigidity [13, 14]. Key of this cellular mechano-response is the transcriptional regulator YAP/TAZ [15-18]. Once activated by mechanical cues, YAP/TAZ translocate into the nucleus and thereby drive gene expression through binding to multiple transcriptional factors that e.g. control cell survival, proliferation, cell fate, and metabolic wiring [14, 16, 19]. Importantly, YAP/TAZ plays an essential role in stemness regulation during embryonic development [20-25]. Hence, transient expression of YAP/TAZ by mechanical stimulation, can reprogram differentiated cells into their corresponding stem or progenitor status [24]. In cancer, active YAP/TAZ is reported to promote cancer stemness in breast cancer, osteosarcoma and glioblastoma [26-28]. Bioinformatic genome analysis identified that PCa patients derived CSCs have significantly enhanced expression of TAZ together with gene signatures for enhanced focal-adhesion and cell-ECM interactions. Those results imply the close relation between focal adhesions, cytoskeletal tension, TAZ activation and PCa cancer stemness.

In order to understand the role of focal adhesions, cytoskeleton remodeling and mechano-responses in regulation of PCa cancer stemness-regulation and metastasis initiation, we here combined experiments on the mechanical responses of single PCa cells to matrix stiffness with measurements of the cellular force generation as readout of cytoskeletal tension, and the metastatic potential of PCa CSC-like cells (CSC-LCs) in zebrafish/mice xenografts and human organoids. The integrated approach allowed us to demonstrate that the metastatic potential of CSC-LCs relies on their anomalous mechanotransduction ability. Mechanotransduction, mediated by integrin β1 and integrin-linked kinase (ILK) leads to significant cytoskeleton remodeling through CDC-42-N-Wasp-Cortactin axis, increase of cytoskeletal tension that results in nuclear translocation of TAZ, the latter driving expression of pluripotency genes, a prerequisite to metastatic tumor initiation. Suppression of this signaling cascade significantly attenuated metastasis initiation in both zebrafish and mice xenografts and it blocked near-patient organoid growth. Overall, our study underscores the essential role of integrin-dependent mechanotransduction of CSC-LCs in PCa metastasis, and suggesting the pathway as future therapeutic target.

Materials and methods

Cell culture, *in vitro* treatment and WST assay

Human embryonic kidney cells HEK-293T (kindly provided by Dr. Sylvia Le Dévédec, LACDR, Leiden) were maintained in DMEM supplemented with 10% FCS. Human PCa cell lines PC-3 and PC-3M-Pro4-luc2 (kindly provided by Dr. Gabriel van der Pluijm, Department of Urology, LUMC) were maintained in Nutrient Mixture F-12K supplemented with 10% FCS and DMEM supplemented with 10% FCII (Hyclone™), respectively. C4-2B were maintained in low-glucose DMEM supplemented with 20% Ham's F-12K, 10% FCS, 1x ITS Liquid Media Supplement (Thermo Fisher Scientific), 13,6pg/ml T3, 0,25ug/ml Biotin and 25ug/ml Adenine. All medium are obtained from Gibco™. For mechano-responding measurement, cells were seed on elastic cell culture substrates with defined stiffness (2, 15 or 100kPa) (ExCellness) coated with type I

collagen (Sigma-Aldrich). Matrigel on top (MoT) 3D culture was performed as previously described [11]. In brief, 200 cells were seed in each well of 8-well chambers coated with a thick layer of matrigel (Thermor Fisher Scientific) and covered with 200 ul full-medium containing 3% matrigel. For *in vitro* treatment, 6000 cells suspended in full medium were seed in each well of 96-well plates (6000 cells/well). After 24 hours the medium was replaced with low-serum medium (3% serum) containing Vehicle control (Veh), Integrin α2β1 inhibitor BTT3033 (TOCRIS), ILK inhibitor CPD22 (Millipore) and/or YAP/TAZ inhibitor Verteporfin (Sigma-Aldrich). Cell proliferation was assessed after 72hours of treatment using Cell Proliferation Reagent WST-1 (Roche) following the manufacturer's protocol. 10ul WST reagent was added into each well. After 2 hours of incubation at 37 ˚C, the plate was measured with microplate reader M1000 PRO (TECAN). Each condition was repeated 6 times in two independent experiment.

Cloning, lentivirus production and transduction

Short hairpin RNA (shRNA) constructs were obtained from Sigma's MISSION library (Kindly provided by Department of Molecular Cell Biology, LUMC). pDEST/Lifeact-mCherry-N1 was a gift from Robin Shaw (Addgene plasmid # 40908), pmCherry Paxillin was a gift from Kenneth Yamada (Addgene plasmid # 50526) and pmCherry Paxillin (#50526) and pLL3.7 EGFPC2 TAZ was a gift from Yutaka Hata (Addgene plasmid # 66850). Lifeact-mCherry-N1 and mCherry-Paxillin were amplified by PCR and cloned into pLenti-blasticidin (kindly provided by Dr. Maciej Olszewski). Lentivirus were produced by transforming pLenti constructs, packaging plasmids psPAX2 and enveloped plasmids pMD2.G (a gift from Dr. Maciej Olszewski) into HEK-293T cells using lipoD293 (SignaGen Laboratories) as transforming reagent. Lentivirus supernatant was collected at 72hour after transformation. Cells were transduced with the lentiviruses using 6ug/ml Polybrene (Sigma-Aldrich).

ALDEFLUOR assay and FACS sorting

The cellular subpopulation with high Aldehyde dehydrogenase (ALDH) activity was selected using ALDEFLUOR Assay kit (StemCell technology) following the manufacturer's protocol. In brief, 1-10 million PC-3M-Pro4-Lifeact-mCherry were labelled with the ALDEFLUOR reagent. For negative control, 500,000 PC-3M-Pro4-Lifeact-mCherry cells were firstly treated with ALDEFLUOR reagent and immediately mixed with ALDH inhibitor TEAB. These cells were used to gate the negative population. FACSCanto II and FACSAria III cell sorter (BD Biosciences) were used for the measurement and sorting. Data was analyzed with FCS Express Software (De Novo Software). Each condition was independently repeated 3 times.

Micropillar-based traction force microscopy

Cellular traction force measurements were performed using elastic micropillar arrays produced in our labs. A hexagonal array of poly-di-methyl-siloxane (PDMS, Sylgard 184, Dow Corning) micropillars of 2 um diameter, 4 um center-to-center distance and with a height of 6.1 um (Young's modulus 28.1 kPa effective stiffness), 4.1 um (49.6 kPa effective stiffness) or

3.2 um (142 kPa effective stiffness) were produced using replica-molding from a silicon wafer [29]. The pillar arrays were flanked by integrated 50 um high spacers to allow the inversion onto glass coverslips, without compromising the limited working distance of a high-NA objective on an inverted microscope. The tops of the micropillars were coated with a mixture of unlabeled and Alexa Fluor 647-labeled fibronectin (1:5, Life Technologies) using micro-contact printing. The position of the pillar tops was observed by confocal fluorescence microscopy and determined down to sub-wavelength accuracy using custom software (Matlab, Mathworks). Forces were obtained by multiplying the pillar deflections by the array's characteristic spring constant (41.2 nN/um, 65.9 nN/um, and 191.4 nN/um, respectively, determined by finite element modeling). The pillars' spring constants were converted to an equivalent Young's modulus for continuous substrates [30] of 29.5 kPa (soft pillars), 47.2 kPa (medium pillars) and 137.1 kPa (stiff pillars), respectively. Only pillars closer to the cell perimeter than 3 um and with a deflection >65 nm for soft pillars, >70 nm for medium pillars, and >75 nm for stiff pillars were considered for the calculation of the total cellular forces. The deflection thresholds, which reflect the positional accuracy by which individual pillars could be localized, were determined for each confocal image as the 75th percentile of the displacements of pillars outside the cell area (i.e. not bent by the cells). The cell spreading area (A) and perimeter (p) were determined by thresholding the fluorescence signal of Alexa Fluor 532-Phalloidin labeled actin filaments using a triangular threshold method [31]. The (unitless) cell elongation was calculated as $p^2/(4pA)$.

Micropillar imaging was performed on a home-built setup based on an Axiovert200 microscope body (Zeiss). Confocal imaging was achieved by means of a spinning disk unit (CSU-X1, Yokogawa). The confocal image was acquired on an emCCD camera (iXon 897, Andor). IQ-software (Andor) was used for basic setup-control and data acquisition. Illumination of Alexa Fluor 532-Phalloidin and Alexa Fluor 647-fibronectin was performed with two different lasers of wavelength 514 and 642 nm (Cobolt and Spectra, respectively). Accurately controlled excitation intensity and excitation timing were achieved using an acousto-optic tunable filter (AA Optoelectronics). Light was coupled into the confocal spinning-disk unit by means of a polarization maintaining single-mode fiber (OZ Optics). The fluorescent signal was collected by a 40X/1.3 or 100X/1.4 oil objectives (Zeiss).

Cytoimmunofluorescence

2D or 3D (MoT) cultured cells in 8 wells chamber were fixed with 4% PFA (Sigma-Aldrich) in PBS and permeablized with 0.5% triton-X 100 in PBS. After incubation with blocking buffer containing 5% BSA in PBS, the cells were incubated with primary antibody overnight at 4 ˚C and with fluorescent conjugated secondary antibody, Phalloidin and Dapi (Thermo Fisher) for 45 min at room temperature. Images were acquired using a Leica SP8 confocal microscope (Leica) or Nikon Eclipse Ti confocal laser-scanning microscope (Nikon). Primary antibodies used in the research included rabbit anti-human TAZ, anti-human ILK, anti-human

phosphorylated Paxillin (Cell Signaling Technology) and anti-humanKi67 (Abcam). Images were processed and analyzed using imageJ software.

Zebrafish maintenance, tumor cell implantation and metastasis analysis

Wildtype zebrafish (ZF) line ABTL and transgenic line tg (Fli:GFP) were handled in compliance with local animal welfare regulations and maintained according to standard protocols (www.ZFIN.org) [32].

Cancer cell transplantation was performed as described before[33-35]. Briefly, two days post-fertilization (dpf), dechorionated ZF embryos were anaesthetized with 0.003% tricaine (Sigma) and plated on a Petri dish covered with 1.5% of solidified agarose. Cancer cells were trypsinized, suspended in PBS containing 2% polyvinylpyrrolidone (PVP; Sigma-Aldrich) with a concentration of 100,000 cells/ul and loaded in into borosilicate glass capillary needles (1 mm O.D. × 0.78 mm I.D.; Harvard Apparatus). 300-500 cancer cells were injected into duct of cuvier (DoC) of ZF embryos using a Pneumatic Picopump and a manipulator (WPI). The injected embryos were further maintained in a 34 ˚C incubator. Images were acquired with a Leica M165 FC stereo fluorescent microscope at 1-, 2-, 4- and 6- days post injection (dpi). Data was further analyzed with image J software and/or ZF4 pixel counting program (Leiden). For high resolution imaging, zebrafish embryos were placed on glass-bottom petri dishes and covered with 1% low melting agarose containing 0.003% tricaine (Sigma). Images were acquired using a Leica SP8 confocal microscope (Leica) or Nikon Eclipse Ti confocal laser-scanning microscope (Nikon) and analyzed with image J software.

Western blot

Protein samples were collected by lysing cells with lysis buffer containing phenylmethanesulfonyl fluoride (Cell Signaling Technology) and were separated by SDS-PAGE (Bio-Rad). After transferred to polyvinylidene difluoride membranes (Millipore), the samples on the membranes were incubated with primary antibody (1:1000 times dilution) followed by horseradish peroxidase-labeled secondary antibodies (1:1000 times dilution). After treating with enhanced chemoluminescence substrate mixture (Cell Signaling Technology), blots were scanned with ChemiDoc XRS+ System (Bio-rad). Primary antibodies rabbit anti-human ITGB1, anti-human ILK, anti-human paxillin, anti-human phosphorylated YAP/TAZ (ser127/Ser89), anti-human LATS, anti-human phosphorylated LATS, anti-human MST, anti-human phosphorylated MST, anti-human Nanog and anti-human Oct-4 were obtained from Cell Science Signaling. Rabbit anti-human GAPDH and mice anti-YAP are obtained from Santa Cruz Biotechnology.

RNA isolation and qPCR

Whole RNA was isolated using RNeasy Mini Kit (Qiagen) following the manufacturer's introduction. cDNA synthesis and qPCR was performed using qPCR, iScript™ cDNA Synthesis Kit (Bio-rad) and iQ™ SYBR® Green Supermix (Bio-rad) following the manufacture’s protocol.

Data was analyzed using 2-ΔΔct method and results were normalized to the expression level of GAPDH and/or β-actin.

Clonogenicity assay

Single cell suspensions were seeded in 6-well plates (200 cells/well) covered with 1.5ml completed medium. After 10-14 days culturing, the cells were fixed with 4% Paraformaldehyde (PFA) and stained with 10% crystal violet (Sigma). Images were acquired using ChemiDoc XRS+ System (Bio-rad) and analyzed with image J software.

Tumor spheroid assay

1000 single cells were suspended in 50% matrigel and seeded in a 24 wells ultra-low binding plates covered with 200uL completed medium. Number of tumor spheres was counted after 10 days culturing.

Mice experiment

5-6 weeks old male CB17 SCID mice were obtained from Charles River (L'Arbresle, France) and housed in sterile ventilated cages. Sterile food and water was provided *ad libitum*. Animal experiments were conducted following Swiss Guidelines for the Care and Use of Laboratory Animals under the license BE55/16 approved by the local committee for animal health ethics and research of the Canton Bern, Switzerland. Intra-osseous (IO) experiments were performed as previously described. 50.000 PC-3M-Pro4-LUC2-Lifeact-mCheery containing either ITGB1 kd or SCR non-targeting control were injecting in the left tibia of the mice. BLI imaging (NightOwl, Berthold, Bad Wildbad, Germany) and X-ray assessment (Faxitron Bioptics, Tucson, Arizona, US) at day 7, 14 and 28 after implantation were conducted respectively to track cell growth and bone lesions progression. 5 mice were used for each experimental group.

Organoids culture

Patient-derived PCa (CRPC) cell LAPC9 was maintained in male CB17 SCID mice as described before. Cancer tissues were dissociated with collagenase and single cells were seeded in ultra-low attachment 6-well plates with a density of 50,000 cells/well covered with DMEM/F-12 medium supplemented with 5% FCS, Hepes, primocin, GlutaMAX, Y-27632, A83-01, SB202190, R-Spondin, Noggin, B27, N-acetyl-cysteine, Nicotinamide, EGF, FGF10, FGF2, DHT, Wnt3A, HGF and PGE2.

Statistics

Statistics analysis was performed with a Graphpad Prism 7.0 software. t-Test was used to compare two groups and ANOVA for multiple groups. Data is presented as mean ±SEM or mean ±SD. p-values ≤0.05 are considered to be statistically significant (*p≤0.05, **p<0.01, ***p<0.001, ****P<0.0001)

Results

PCa CSCs have stronger response to matrix stiffness controlling cytoskeletal tension, TAZ activation and CSC maintenance

We compared TAZ expression in PCa metastases and the correlated primary site, in 2 different clinical datasets (Taylor Prostate (181 primary tissues and 37 metastasis tissue) and Grasso Prostate (59 primary tissues and 35 metastasis tissues) [36, 37]). In both datasets, the PCa metastases displayed a significantly enhanced TAZ expression (Fig. 1a). Next we compared TAZ expression in patients CSCs and non-CSCs (7 benign tissues and 9 PCa tissues, [2]). Interestingly, in the CSC population of PCa rather than benign tissues, the expression of TAZ was significantly upregulated (Fig. 1a). Overall, our clinical datasets analysis suggests a close correlation between mechanotransduction, cancer stemness and PCa metastasis.

We therefore directly assessed the correlation between mechanotransduction and CSC-like phenotypes by seeding osteotropic PCa cells PC-3M-Pro4 on elastic substrates with defined stiffness: 2kPa, 15kPa and 100kPa. Given that TAZ is nuclear when cells sense increased matrix stiffness[38], we determined by immunofluorescence TAZ intensity in the nucleus and in the cytoplasm (Fig. 1d). 80% of the cells growing on 100kPa showed higher TAZ intensity in the nucleus than in the cytoplasm while only 50% of the cells on 2kPa had stronger TAZ nuclear signal (Fig. 1e). Additionally, the ratio of nuclear to cytosolic TAZ intensity was significantly elevated in the cells on 100kPa compared to the 2kPa ($p<0.001$) (Fig. 1e), indicating that PCa cells can respond to the increased stiffness, and allow TAZ nuclear translocation. We next questioned if CSC-like phenotype of PCa cells was influenced by the different stiffness. Given that the cell subpopulation with high Aldehyde Dehydrogenase (ALDH) activity has been defined as a CSC-enriched cell fraction [39], we measured the size of $ALDH^{hi}$ subpopulation in PC-3M-Pro4 after being exposed to different stiffness. The $ALDH^{hi}$ fraction was increased to 30% on 100 kPa from 5% on 2kPa and 9% on 15kPa (Fig. 1f). In addition, the cells on 100kPa had significantly higher expression of pluripotency genes NANOG, OCT4 and SOX2 (Fig. 1g). To further address the correlation between mechanotransduction and stemness, the mechanical responses between $ALDH^{hi}$ and $ALDH^{low}$ subpopulation were compared. Directly after FACS sorting, both cell fractions were seeded on fibronectin-coated elastic micropillar substrate with a low (28kPa) or high (142kPa) stiffness (Fig. 1h) [29]. The cell spreading area, elongation and contractile force generated by the cell-ECM interaction were measured. The $ALDH^{hi}$ cells showed elevated spreading and elongation on the rigid substrate associated with a significantly enhanced contractile force generation (Fig. 1h). Next, we seed both cells for Matrigel on top (MoT) 3D culture, an *in vitro* 3D assay to mimic cancer cell metastatic colonization [40]. We compared TAZ nuclear translocation between the two subpopulations: $ALDH^{hi}$ cells had significantly enhanced TAZ nuclear translocation compared to the $ALDH^{low}$ accompanied by formation of Filopodia-protrusions (FLPs) (Fig. 1i). Taken together, these results suggest a strong link between focal adhesion, cytoskeleton remodeling, mechanotransduction and CSC-like phenotype regulation.

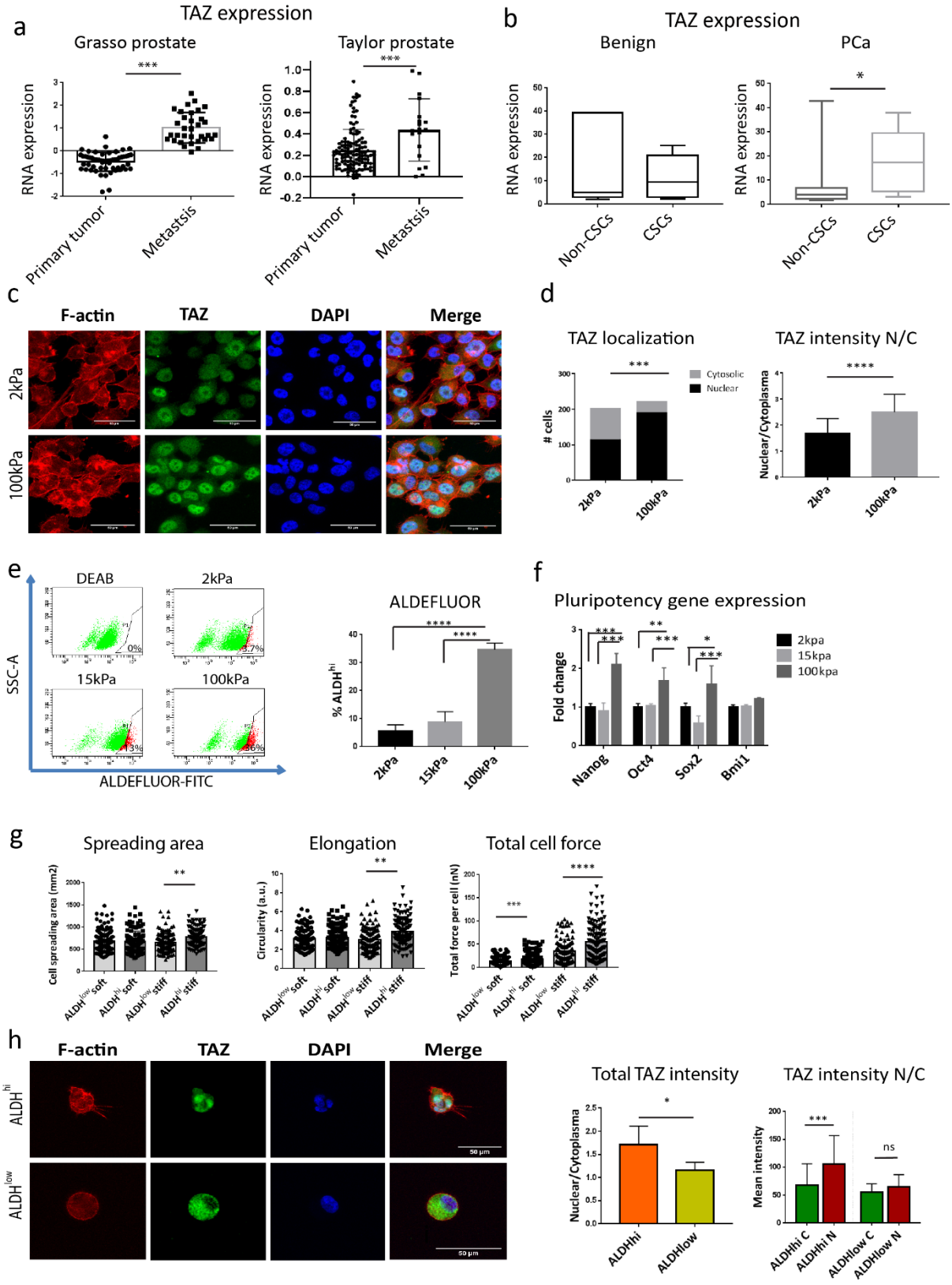

Fig. 1 PCa CSC-like phenotype correlates with enhanced cell contractility and TAZ nuclear translocation. (a) TAZ expression was compared between PCa metastases and the primary site. Clinical datasets Taylor Prostate (GSE21032) and Grasso Prostate (GSE35988) were used for the analysis (data accessed from www.oncomine.org). (b) TAZ expression was compared between CSCs and non-CSC. ArrayExpress Database (accession E-MEXP-993) was used for the analysis. (c-d) PC-3M-Pro4 cells were seeded on elastic cell culture

substrates with stiffness of 2kPa and 100kPa for 48 hours. Immunofluorescence against TAZ was performed. TAZ signal intensity in cytoplasm and nucleus was analyzed using an Image-J program. Group size = 30. (e-f) PC-3M-Pro4 were seeded on 2kPa, 15kPa and 100kPa for 96 hours. Size of ALDHhi subpopulation (e) and expression of pluripotency genes (f) were measured. Experiments were independently repeated 3 times. (g) ALDHlow and ALDHhi subpopulations were seeded on elastic micro-pillar arrays with low (28kPa) and high (142kPa) stiffness for 24 hours. Cell spreading area, Elongation and Contractile force were measured. 120 cells from 3 independent experiments were analyzed for each group. (h) ALDHlow and ALDHhi subpopulations were seeded in MoT 3D culture. Immunofluorescence against TAZ was conducted. TAZ intensity in nucleus and in cytoplasm was calculated. Scare bar = 50um. Group size = 30. *p<0.05, **p<0.01, ***p<0.001, ****p<0,0001. Arrow bars are s.e.m.

ALDH^{hi} subpopulation display enhanced extravasation and metastatic tumorigenicity associated with elevated cytoskeleton remodeling and integrin expression

Given that focal adhesion transduces mechano-signals through cytoskeleton organization[15], we next applied a zebrafish xenograft model to image cancer cell focal adhesion and cytoskeleton organization at the initial stage of metastasis. We transduced osteotropic PCa cells PC-3 and PC-3M-Pro4 with Lifeact-mCherry, a small fluorescent peptide labelling actin filaments, and intravenously injected these cells into ZF embryos at 2 days post fertilization (2dpf) [41]. Once introduced, the cells migrated through the vascular network, extravasated (Movie. S1) and formed perivascular metastases at the caudal hematopoietic tissue (CHT) accompanied by cytoskeleton remodeling (Fig. 2b, S1a). To trace the actin cytoskeleton organization of the single cancer cells, we co-injected PC-3M-Pro4-Lifeact-mCherry with PC-3M-Pro4-GFP into ZF. At 3 hour post injection (hpi), rounded cancer cells were circulating in the vasculature (Fig. 2b). At 1-2 days post injection (dpi), the cancer cells that homed to the metastatic site (CHT) showed filopodia and/or invadopodia-like protrusions leading the extravasation (Fig. 2b, S1a). By 3dpi the cancer cells further spread and formed stress fibers (Fig. 2b). Those cells eventually acquired an elongated mesenchymal-like morphology leading the invasion at 6 dpi (Fig. 2b, S1a, Movie. S2). To further understand the cell dynamics during metastasis, we analyzed the transcriptomics of PC-3M-Pro4 in culture and in vivo after extravasation. The gene signatures for focal adhesion and ECM-receptor interaction were significantly elevated in metastases (Fig. S1c). Consistently, focal-adhesions plaques at the metastatic onset were visualized through ectopic expression of the focal-adhesion marker Paxillin-mCherry into PC-3M-Pro4 [42] (Fig. S1d).

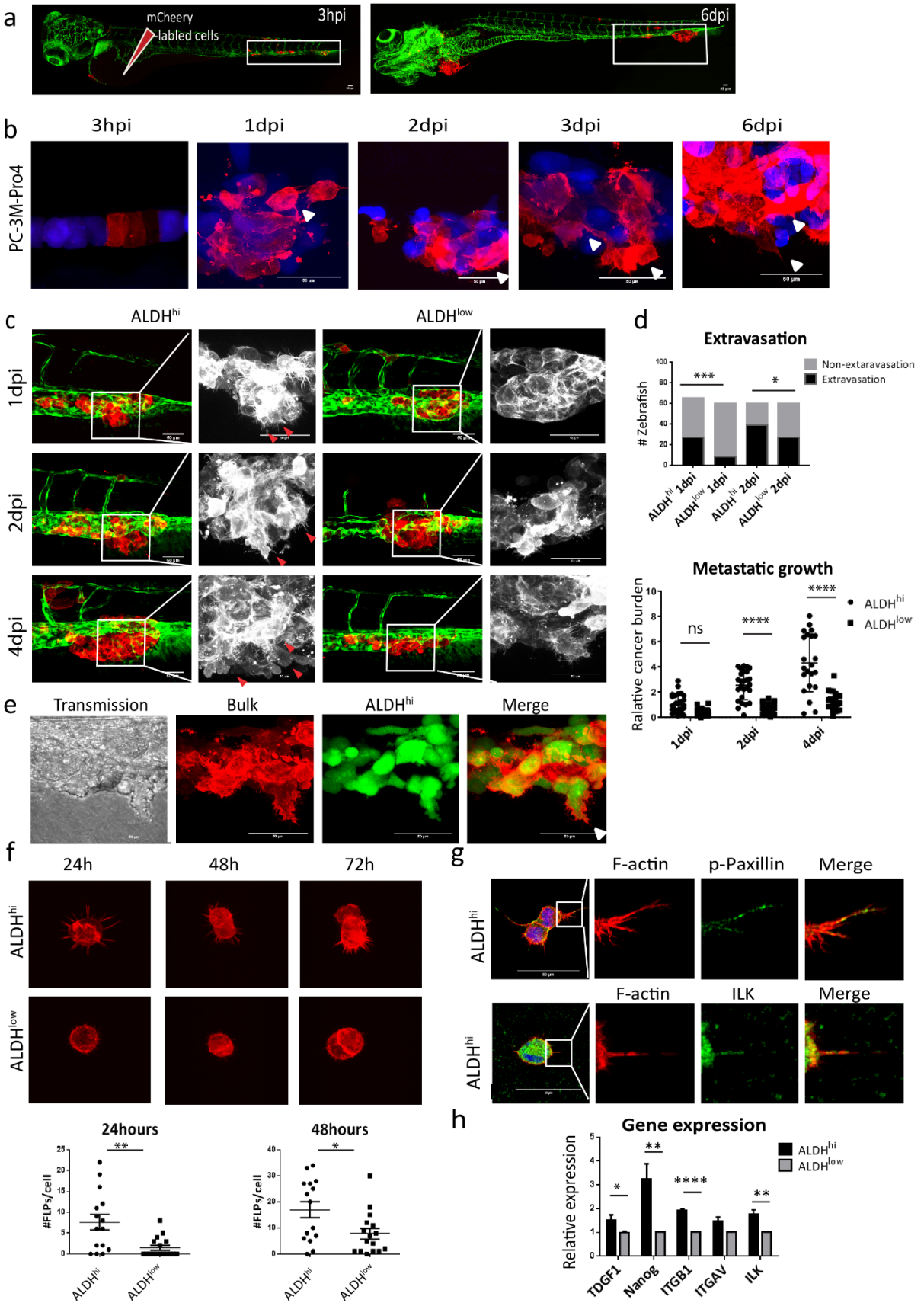

Fig. 2 ALDH^{hi} subpopulation display enhanced extravasation and metastatic outgrowth associated with elevated focal adhesion and actin dynamics in ZF xenografts and in MoT 3D culture. (a) Scheme of intravenous transplantation of PCa cells into ZF. PCa cells were stably expressed with Lifeact-mCherry and injected into duct

of cuvier (DoC) at 2 days post fertilization (2dpf). Perivascular metastases at CHT area (white box) was developed at 6 days post injection (dpi) (red, cancer cells; green ZF vessel). (b) Visualization of cytoskeleton dynamics of PC-3M-Pro4-Lifeact-mCherry during metastasis initiation. PC-3M-Pro4-LLifeactifeact-mCherry (red) was mixed with PC-3M-Pro4-GFP (blue) and co-injected into ZF. Confocal images were acquired at 1, 2, 3 and 6 dpi. Scale bar = 50uM. White arrow, invasive cells. (c-d) Comparison of metastatic behavior of $ALDH^{hi}$ and $ALDH^{low}$ cells in ZF. (c) Both cell subpopulations were isolated from PC-3M-Pro4-Lifeact-mCherry and respectively injected into ZF. Confocal images were acquired at 1, 2 and 4 dpi. Green, ZF vessels; Red, cancer cells; White, enlargement of the cancer cells. Scale bar= 50um. For extravasation analysis, % of ZF with more than one cells extravasated from the vessels and invaded into neighboring tissues around CHT area was counted (60 fish per group). For proliferation analysis, intensity of total mCherry fluorescence at CHT area were measured using a ZF pixel counter program (n=30). (e) Localization of $ALDH^{hi}$ cells in the bulk population at the early stage of metastasis in ZF. $ALDH^{hi}$ subpopulation was stained with CSFE dye and co-injected with the $ALDH^{low}$ cells into ZF. Confocal images were acquired at 2dpi. $red^{+}/green^{-}$, $ALDH^{low}$ cells ; $red^{+}/green^{+}$, $ALDH^{hi}$ cells. Scale bar=50um. White arrow, invasive cells. (f) The $ALDH^{hi}$ and $ALDH^{low}$ cells from PC-3M-Pro4-Lifeact-mCherry were seed on matrigel, number of Filopodia-like protrusions (FLPs) (length>10um) was counted at 24 and 48 hour after seeding. 15 cells were counted in each condition. Experiments were independently repeated 2 times. (g) Immunofluorescence against p-Paxillin and ILK was performed on $ALDH^{hi}$ cells in MoT culture to detect co-localization of FLPs and p-Paxillin and ILK. Scale bar=50uM. (h) Expression of stemness markers, integrins and ILK were compared between the $ALDH^{hi}$ and $ALDH^{low}$ cells. Experiments were independently repeated 3 times. Group size = 30. *p<0.05, **p<0.01, ***p<0.001, ****p<0,0001. Arrow bars are s.e.m.

Since $ALDH^{hi}$ subpopulation has stronger metastatic potential than its $ALDH^{low}$ counterparts [39], we next compared the cytoskeleton behaviors of $ALDH^{hi}$ and $ALDH^{low}$ subpopulations. The $ALDH^{hi}$ and $ALDH^{low}$ cells were sorted from bulk PC-3M-Pro4-Lifeact-mCherry and respectively injected into ZF. Within the first 2 days, the $ALDH^{hi}$ cells formed filopodia/invadopodia-like protrusions leading the extravasation and invasion (Fig. 2c). The percentage of ZF with more than one cells extravasating and invading neighboring tissues were counted (Fig. 2d). At 1dpi we observed a remarkable difference in the extravasation potential of the two cell populations (30% of $ALDH^{hi}$ vs 8% of $ALDH^{low}$ cells). At 2dpi the gap between the $ALDH^{hi}$ and $ALDH^{low}$ fraction was reduced but still statistically significant. In addition, the transplantation of $ALDH^{hi}$ cells induced a significantly enhanced cancer cell burden (calculated as total fluorescence) at the CHT area at 2 and 4dpi, indicating a stronger metastatic tumor growth (Fig. 2d). To specifically trace the behavior of $ALDH^{hi}$ cells in the bulk population, $ALDH^{hi}$ –Lifeact-mCherry cells were stained with green CSFE, a FITC dye labelling cytoplasmic amine residues, and co-injected into ZF with the $ALDH^{low}$–Lifeact-mCherry cells. The $ALDH^{hi}$ cells (double-positive for both FITC and Lifeact-mCherry) gained elongated mesenchymal-like phenotype and were mostly localized at the invasive front of the cancer cell burden (Fig. 2e).

Additionally, we checked the cytoskeleton remodeling of the cancer cells in 3D MoT culture [11, 40]. When the $ALDH^{hi}$ and $ALDH^{low}$ cells were seeded on matrigel with a low cell density, significantly enhanced number of FLPs were formed in the $ALDH^{hi}$ cells at 24 and 48 hours (Fig. 2f). Immunostaining showed that the FLPs were enriched in the focal adhesion markers p-Paxillin and integrin-linked kinase (ILK) (Fig. 2g). By qPCR, $ALDH^{hi}$ cells had enhanced

expression of adhesion molecules Integrin β1 (ITGB1), Integrin αV (ITGAV) and ILK, suggesting an increase of focal adhesion and cytoskeleton organization (Fig. 2h).

Integrin β1 and ILK knockdowns inhibit focal adhesion, CSC-like phenotype and FLPs formation *in vitro*

ILK is a interactor of Integrin β1, which transduces focal adhesion signals into cytoskeleton [43]. To address if this integrin signaling controls the CSC-like phenotype, we employed RNA interference approach to inhibit Integrin β1 and ILK expression. Both knockdowns strongly inhibited Paxillin phosphorylation and stress fiber formation, underlining the involvement of integrin signaling in focal adhesion formation and actin polymerization (Fig. 3a, 3b). We next assessed the effects of ITGB1 kd and ILK kd on the CSC markers (Fig. 3c-3e). Both knockdowns significantly suppressed the expression of pluripotency genes NANOG, OCT4 and BMI1 by more than 70% ($p<0.001$) (Fig. 3c). The percentage of $ALDH^{hi}$ cells was significantly reduced in both knockdowns (Fig. 3d). Additionally, ITGB1 kd and ILK kd significantly suppressed cell clonogenicity and tumorspheroid formation (Fig. 3e, S3a-S3d), indicating integrin β1 and ILK are functionally involved in the CSC-like phenotype regulation. We further measured, by MoT assay, the FLP formation potential of the $ALDH^{hi}$ subpopulation. $ALDH^{hi}$ cells were sorted from SCR, ITGB1 kd1 and ILK kd1 and immediately seeded on matrigel. 24 hours after seeding, FLP formation was significantly reduced in the knockdowns compared to the SCR control ($p=0.018$ for ITGB1 kd and $p=0.0002$ for ILK kd) (Fig. 3f). Altogether, these data propose that integrin dependent focal adhesion regulating cytoskeleton organization controls PCa CSC-like phenotype.

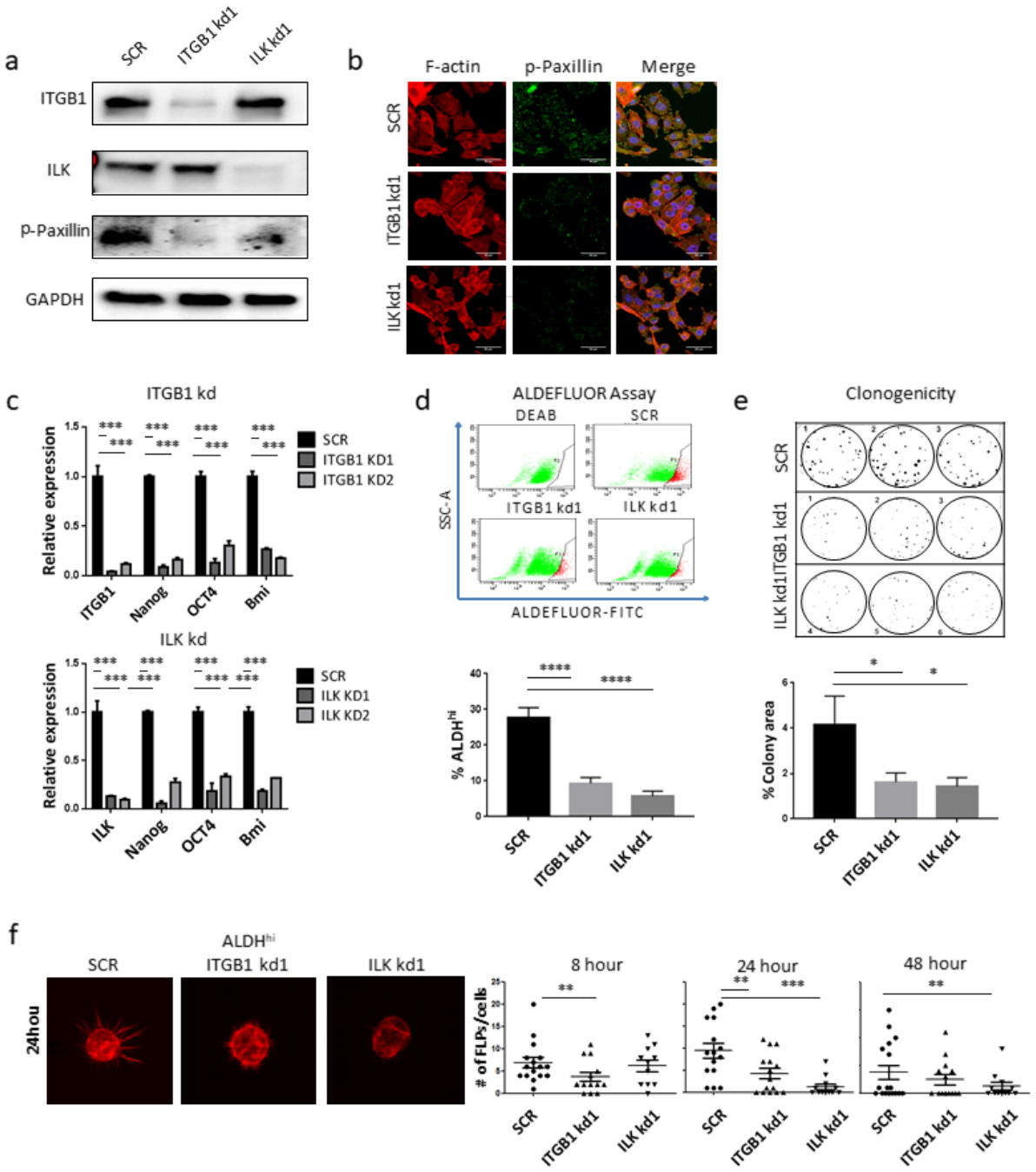

Fig. 3 Knockdown of integrin β1 and ILK inhibits Focal adhesion, cytoskeleton remodeling and CSC-like phenotype. (a-b) Effects of ITGB1 kd and ILK kd on Paxillin phosphorylation. Scale bar=50um. (c-e) Effects of integrin β1and ILK knockdown on the CSC-like properties of PC-3M-Pro4. The expression of pluripotency genes (c), size of ALDH^{hi} fraction (d) and clonogenicity were tested. Each experiment was independently repeated 3 times. (e) Formation of FLPs in the ALDH^{hi} cells isolated from SCR, ITGB1 kd and ILK kd cells. Experiments were individually repeated 2 times, n = 15. *p<0.05, **p<0.01, ***p<0.001, ****p<0,0001. Arrow bars are s.e.m.

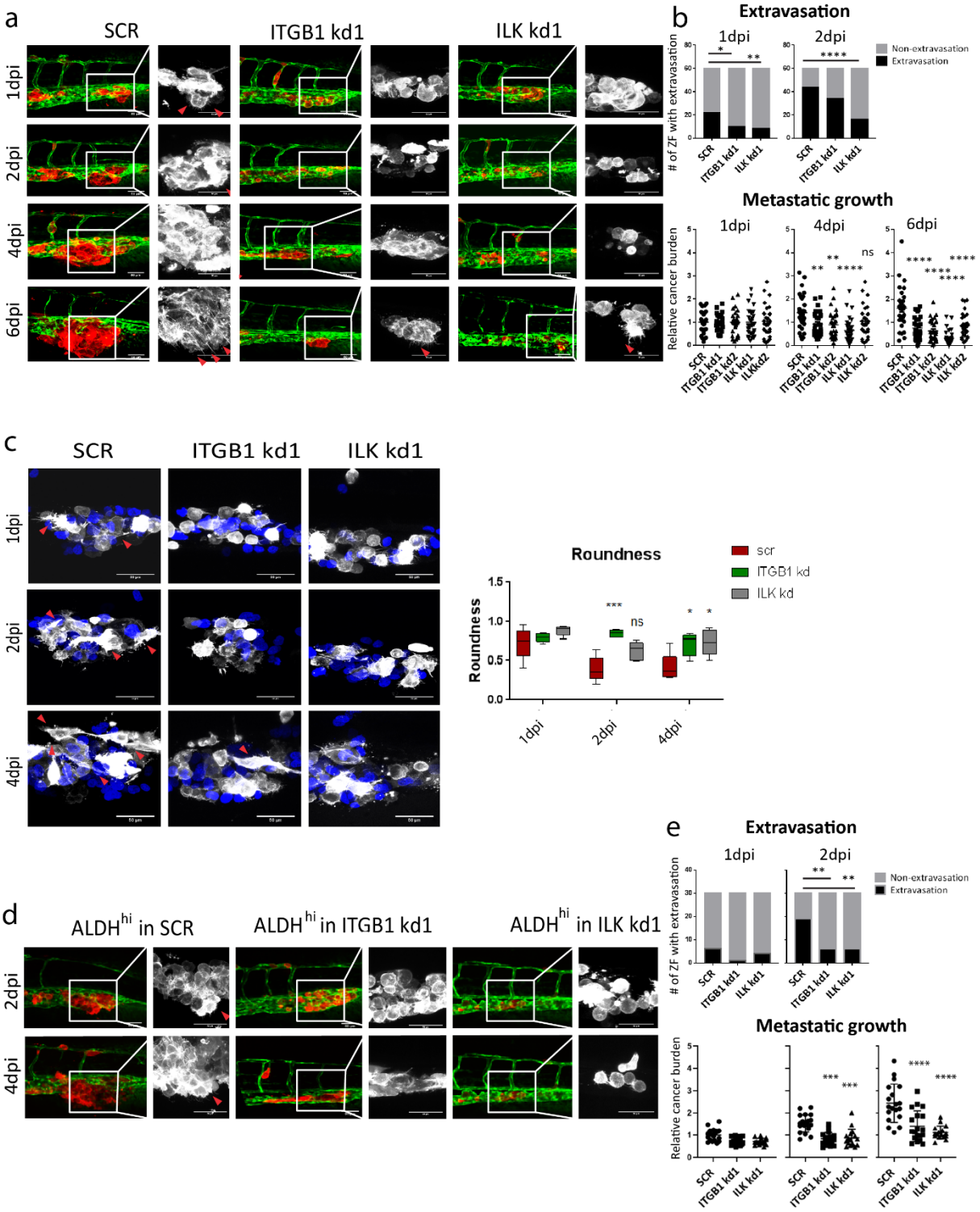

Fig. 4 Knockdown of integrin β1 and ILK suppresses cytoskeleton remodeling and metastasis initiation *in vivo*. (a) PC-3M-Pro4-lifeact-mCherry-SCR, -ITGB1 kd and -ILK kd were respectively injected into ZF. Images were acquired at 1, 2, 4 and 6 dpi. Red arrow, Actin filaments. Scale bar=50um. (b) Extravasation and proliferation of the cancer cells at the metastatic site were analyzed. Group size=30. Experiments were independently repeated 2 times. (c) Analysis of actin dynamics during metastasis initiation. PC-3M-Pro4-Lifeact-mCherry-SCR, -ITGB1 kd1 or -ILK kd1 (white) were co-injected with PC-3M-Pro4-GFP (blue) into ZF. Images were acquired at 1, 2 and 4 dpi. Scare bar=50um. Red arrow, spreading cells. Roundness of the cancer cells was calculated using image J. Group size=10. (d-e) ALDH^{hi} subpopulation was isolated from PC-3M-Pro4-Lifeact-mCherry-SCR, -ITGB1 kd1 or -ILK kd1 and injected into ZF. Actin dynamics of the cells were monitored by confocal imaging. Scale bar= 50um. Extravasation and proliferation of the cancer cells at metastatic site were analyzed. Group size= 20. (f) PC-3M-Pro4-Luc2-SCR and –ITGB1 kd1 were injected into tibia of nude mice. Tumor growth was monitored by bioluminescent imaging

(BLI) at the 7th 14th and 28th day. BLI unite was represent as relative tumor burden. Group size=5. (g) The osteolytic lesion progression induced by PC-3M-Pro4-Luc2-SCR and –ITGB1 kd1was compared using image J. Group size=5. *p<0.05, **p<0.01, ***p<0.001, ****p<0,0001. Arrow bars are s.e.m.

Integrin β1 and ILK knockdowns inhibit cytoskeleton remodeling, extravasation and metastatic tumorigenicity in vivo

Next, we examined the role of Integrin β1 and ILK in metastatic onset, characterized by extravasation and metastatic tumor growth. PC-3M-Pro4 and PC-3 cells containing SCR controls and ITGB1 kd and ILK kd were injected into ZF embryos and the cell cytoskeleton remodeling was monitored by confocal imaging. After injection, the SCR cells adhered to the endothelial vessels, migrated and homed to the caudal vein within 15 hours whereas the ITGB1 kd and ILK kd cells only circulated in the blood flow (Fig. 4a, Movie. S3a, S3b, S4a, S4b). In the following 6 days, the extravasation and proliferation were significantly inhibited by more than 50% in the ITGB1 kd and ILK kd cells accompanied by an attenuation of cytoskeleton remodeling (Fig. 4a, 4b). In order to measure the cytoskeleton remodeling of the individual cells in an heterogeneous population, we co-injected PC-3M-Pro4-iRFP with either PC-3M-Pro4-Lifeact-mCherry SCR control, ITGB1 kd1 or ILK kd1 . All injected cells presented a round morphology at 1 dpi. Interestingly, while the SCR cells shifted to stretched phenotype and had a significant reduction in the roundness by 2-4 dpi (Fig. 4c), the ITGB1 and ILK kd cells morphology was not affected (Fig. 4c). Consistently, in PC-3, both knockdowns significantly inhibited cytoskeleton remodeling and metastatic tumor outgrowth (Fig. S2).

In order to determine if ITGB1 kd and ILK kd have an inhibitory effect on the metastatic potential of $ALDH^{hi}$ cells, we sorted $ALDH^{hi}$ subpopulation from PC-3M-Pro4-SCR, -ITGB1 kd1 and -ILK kd1 cell lines and transplanted into ZF (Fig. 4d). Extravasation was inhibited by 70% in either ITGB1 or ILK knockdown. Additionally, both knockdowns significantly reduced metastatic tumor growth of the $ALDH^{hi}$ cells at the CHT (Fig. 4d, 4e).

Considering the specific osteotropism of prostate cancer cells, we evaluated if ITGB1 kd could impair PC-3M-Pro4 cells colonization of bone tissue. ITGB1 kd cells as well as the control scramble were injected in the tibia of CB57-SCID mice. ITGB1 kd cells displayed a reduction of osteolytic lesion in the intratibial injected mouse model [44] as evident by reduced BLI signal and X-ray assessment (Fig. 4f). Taken together, our studies with two different animal models strongly suggest that integrin signaling plays an essential role in the modulation of the CSC-like phenotype and drives metastatic progression.

Cytoskeleton remodeling mediated by CDC42-N-Wasp-Cortactin axis is required for metastatic tumor initiation

Integrin-dependent cytoskeleton remodeling is a complex process involving numerous proteins [8, 9, 43]. To test if the role of Integrin β1 and ILK in metastasis initiation is mainly dependent on cytoskeleton remodeling, we conducted an *in vivo* shRNA screening using the zebrafish model. In total 8 genes were tested: the small GTPase CDC42, RAC1, the actin

filament regulators Profilin, LIM kinase 1 (LIMK1), the invadopodia/lamellipodia components Wasp, N-Wasp, Cortactin and the filopodia component DIAPH3 (mDIA2) (Fig. 5a). Six out of eight knockdowns significantly suppressed the metastatic tumor outgrowth (Fig. 5b). Notably, the knockdowns of CDC42 and its downstream proteins N-Wasp and Cortactin showed the strongest inhibitory effect at 6dpi associated with reduced cytoskeleton remodeling (inhibition >50%, $p<0.001$) (Fig. 5b-5d, S4). Given that active CDC42 can directly activates N-Wasp dependent F-actin branching leading to the formation of lamellipodia and/or invadopodia [10], we further focused on CDC42 and N-Wasp to determine their roles in metastatic tumor growth.

To unveil if the knockdowns of CDC42 and N-Wasp suppressed metastasis initiation through inhibiting cell division, PC-3M-Pro4-SCR control, -CDC42 kd1 and -N-Wasp kd1 were transduced with fluorescence ubiquitination cell cycle indicator (FUCCI) construct, a cell cycle reporter labelling G0/G1 phase with mCherry and S/G2/M phase with GFP [45], and injected into ZF (Fig. Movie S4). After transplantation, all cells had a similar G/R signal ratio at 1 and 2 dpi (Fig. 5e). Surprisingly, at 4dpi, the G/R ratio was significantly increased in the SCR cells but not in the knockdown cells (Fig. 5e), indicating the SCR cells entered the cell cycle at 4dpi and this cell cycle entry was blocked by the CDC42 and N-Wasp knockdowns.

In parallel, *in vitro* experiments were performed to detect if CDC42 and N-Wasp knockdown affected the CSC-like phenotype of the cells (Fig. S5). ALDEFLUOR assay showed that CDC42 kd significantly suppressed the size of $ALDH^{hi}$ subpopulation. Additionally, both CDC42 kd and N-Wasp kd significantly inhibited the expression of pluripotency genes when the cells were in MoT 3D culture. Moreover, cell clonogenicity and tumor spheroid formation were significantly suppressed by both knockdowns (Fig. S5b-S5d). Taken together, this suggests that cytoskeleton remodeling plays an essential role in CSC-like phenotype regulation and initiation of metastatic tumor growth.

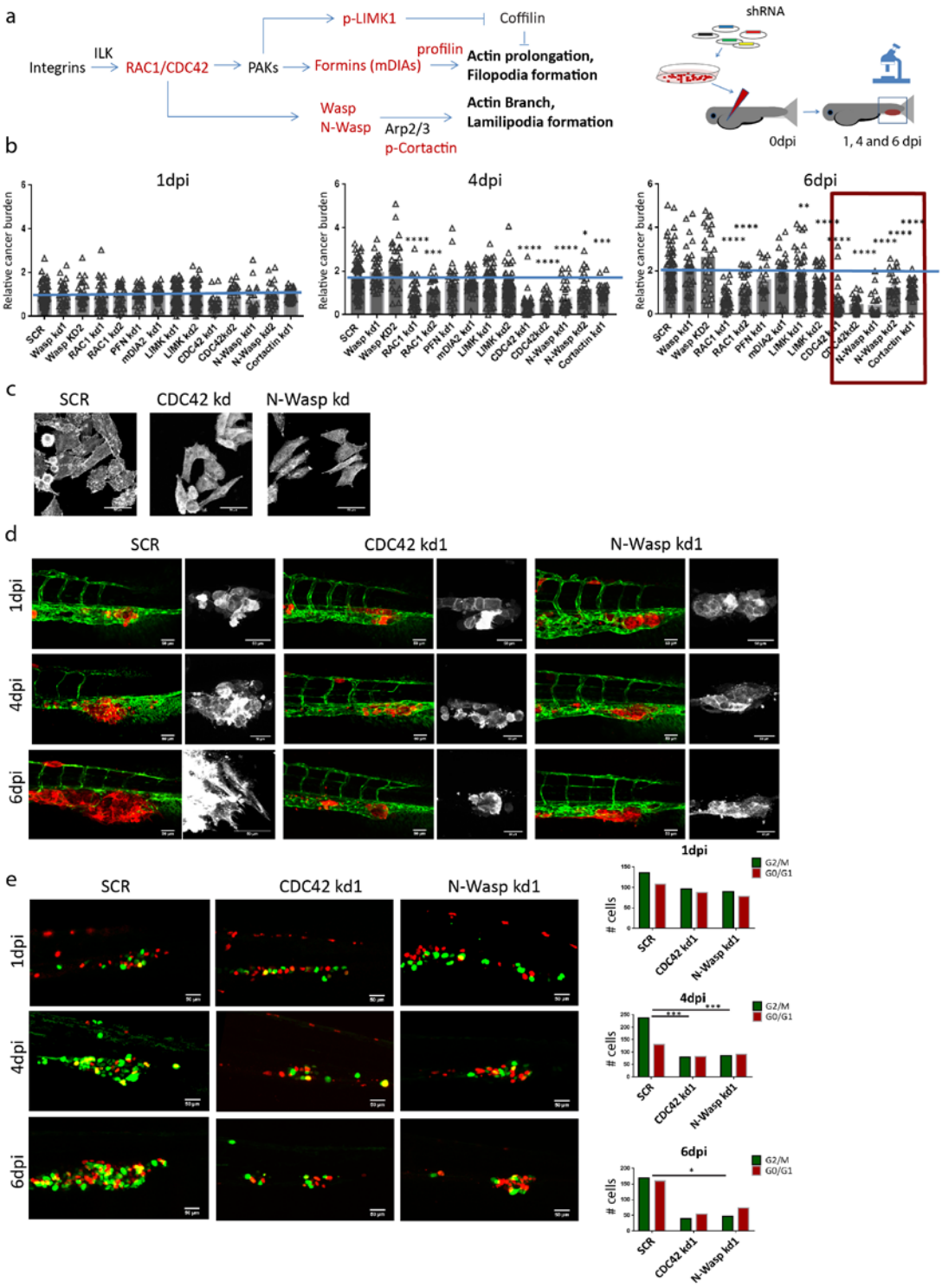

Fig. 5 CDC42-N-Wasp-Cortactin axis is essential for metastatic outgrowth of the PCa cells. (a) Schematic indication of *In vivo* shRNA screening to identify actin factors driving PCa metastasis initiation. Left, scheme of integrin-dependent actin network (red, shRNA targets). Right, scheme of shRNA screening using zebrafish xenograft. PC-3M-Pro4-Lifeact-mCherry containing either SCR control or shRNA against integrin-downstream actin factors were injected into zebrafish. Total cancer cell burden at metastatic site was measured at 1, 4 and 6 dpi. (b) Result of shRNA screening using zebrafish xenografts. Cancer cell burden at the metastatic site was normalized to the total fluorescent intensity at 1 dpi. Each experiment was independently repeated 2 times. Group size = 60. (c) Representative images of PC-3M-Pro4-Lifeact containing SCR, CDC42 kd1 and N-Wasp kd1 on 2D monolayer culture. Scale bar = 50um. (d) Representative images of ZF xenografts with PC-3M-Pro4-Lifeact containing SCR,

injected into zebrafish. Total cancer cell burden at metastatic site was measured at 1, 4 and 6 dpi. (b) Result of shRNA screening using zebrafish xenografts. Cancer cell burden at the metastatic site was normalized to the total fluorescent intensity at 1 dpi. Each experiment was independently repeated 2 times. Group size = 60. (c) Representative images of PC-3M-Pro4-Lifeact containing SCR, CDC42 kd1 and N-Wasp kd1 on 2D monolayer culture. Scale bar = 50um. (d) Representative images of ZF xenografts with PC-3M-Pro4-Lifeact containing SCR, CDC42 kd1 and N-Wasp kd1 at 1, 4 and 6dpi. Scare bar = 50um. Red arrow, elongated invasive cells. (e) Effects of CDC42 and N-Wasp knockdowns on cell cycle process. PC-3M-Pro4-SCR, -CDC42kd and -N-Wasp were transduced with Fucci constructs. After transplantation into ZF, number of green and red cells were counted. 100-300 cells from 5 fish in each group were counted. Left, representative images of the engrafted cancer cells containing Fucci reporter at metastatic site, scale bar = 50um. Right, quantification. Chi-square was used for the analysis. *p<0.05, **p<0.01, ***p<0.001, ****p<0,0001. Arrow bars are s.e.m

Integrin β1-ILK-CDC42-N-Wasp axis mediates mechanical response controlling actin cytoskeletal tension, contractile force generation and Hippo-independent TAZ activation

We next investigated if the Integrin β1-ILK-CDC42-N-Wasp axis modulates the CSC-like phenotype through governing mechanical response and transduction. To measure the intrinsic contractile force of the cells, we seeded the PC-3M-Pro4 cells containing ITGB1 kd1, ILK kd1, CDC42 kd1 and N-Wasp kd1 on micro-pillars array with defined stiffness of 28kPa, 50kPa and 142kPa. At 24 hours after seeding, cell spreading area and contractile force were measured based on the pillars deflection. Following the increase of stiffness, the SCR cells increased cell area from 600 um^2 on 28kPa to 1400 um^2 on 142kPa and generated higher contractile force ranging from 50nN on 28 kPa to 280nN on 142kPa (Fig. 6a-6c). This increase in cell spreading and contractile force generation on 142kPa stiffness was significantly inhibited by the knockdowns of integrin β1, ILK, CDC42 and N-Wasp, suggesting that integrin β1-ILK-CDC42-N-Wasp axis controls actin cytoskeletal tension (Fig. 6a-6c).

Because cytoskeletal tension has been known to drive YAP/TAZ nuclear translocation, we next assessed TAZ nuclear translocation of cells in MoT 3D culture by immunofluorescence. The nuclear translocation of TAZ (and YAP) was significantly attenuated by the knockdowns of Integrin β1, ILK, CDC42 and N-Wasp (Fig. 6d,e, S3a). In addition, both ITGB1 and ILK knockdowns inhibited the expression of TAZ downstream genes: AMTOL, CTGF and CYR61 (Fig. 6e and S3c) while the CDC42 kd only suppressed CYR61 expression (Fig. 6g), indicating that Integrin β1 and ILK had a stronger regulatory effect on TAZ regulation. Consistently, the knockdowns of integrin β1 and ILK also significantly inhibited the nuclear translocation of TAZ in C4-2B (Fig. S6a, S6b).

YAP/TAZ nuclear translocation has been shown to be controlled by either Hippo-dependent or –independent manner [38]. To determine whether the integrin-CDC42-N-Wasp axis controls TAZ activation through Hippo signaling, we measured total protein level of YAP, p-YAP(Ser127), TAZ, p-TAZ(Ser89), LATS1, p-LATS1, MST-1 and p-MST1 by Western blot. Total YAP protein level was reduced in the ITGB1 kd, ILK kd and CDC42 kd cells while the phosphorylation of YAP at Ser127 was not affected (Fig. 6f). For TAZ, neither total TAZ protein level nor TAZ phosphorylation at Ser89 was affected by the knockdowns (Fig. 6f). In addition, the phosphorylation of the Hippo signaling components MST1 and LATS1 was not significantly

affected by the knockdowns (Fig. 6f), indicating the mechanotransduction mediated by integrin-CDC42-N-Wasp axis regulates TAZ nuclear translocation in a hippo-independent manner.

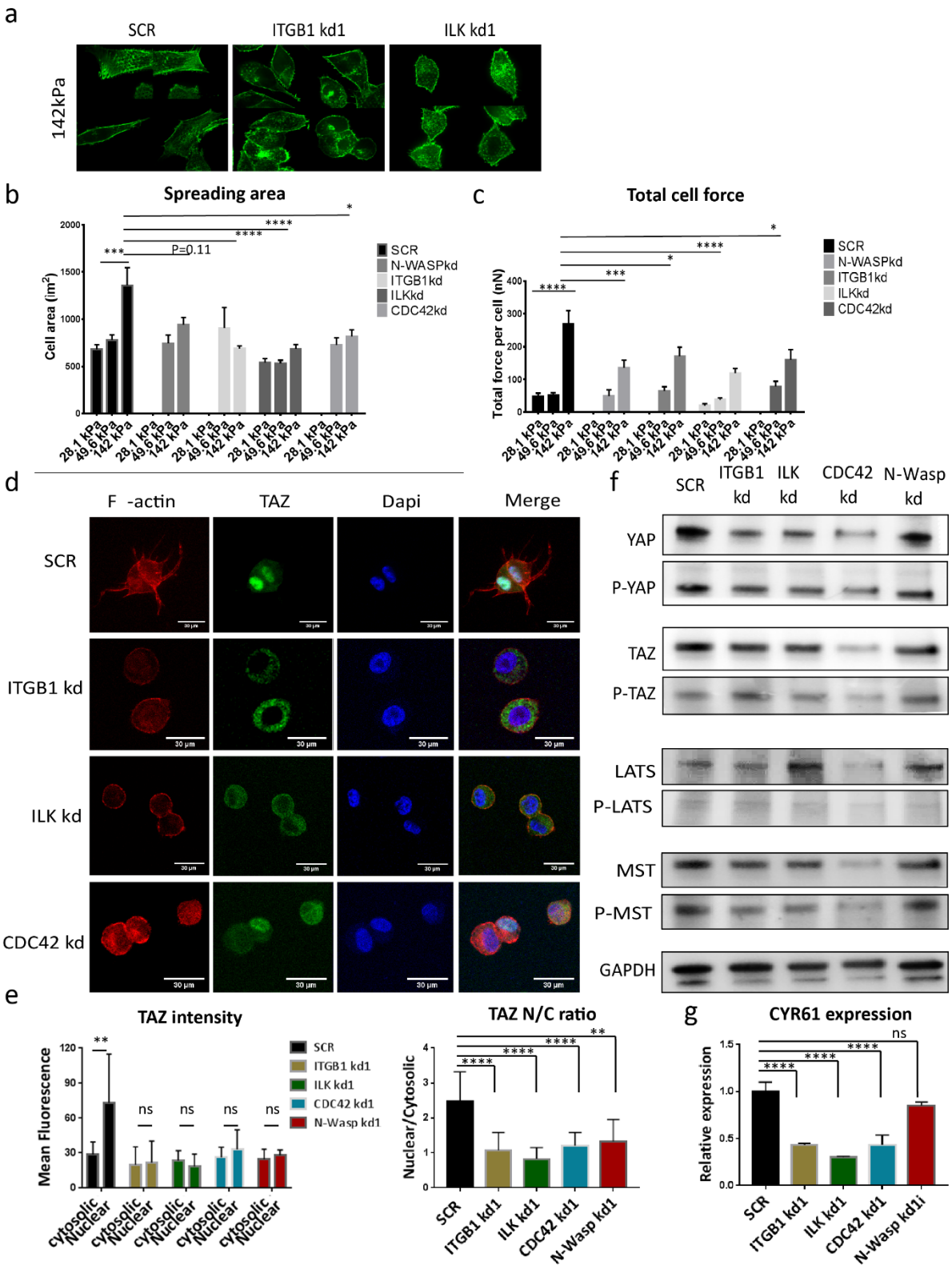

Fig. 6 Integrin β1, ILK, CDC42 and N-Wasp knockdowns inhibit cytoskeletal tension and Hippo-independent TAZ nuclear translocation. (a) Presentative images of PC-3M-Pro4 containing SCR, ITGB1 kd1 and ILK kd1 on elastic

micro-pillar array with a stiffness of 142kPa. (b-c) Spreading area and contractile force of PC-3M-Pro4-SCR, -ITGB1 kd1 , -ILK kd1, -CDC42 kd1 and -N-Wasp kd1 on elastic micro-pillar array. Data was acquired at 24 hours after seeding. 100 cells from 2 independent experiments were measured in each condition. (d) PC-3M-Pro4-SCR, -ITGB1 kd1 , -ILK kd1, -CDC42 kd1 and -N-Wasp kd1 were seed on matrigel for 48 hours. Immunofluorescence was performed against TAZ. Large bar = 50um. (e) TAZ intensity was measure using image-J. Experiments were independently repeated 3 times. 12 cells were measured in each experiment. (f) Analysis of Hippo signaling pathway using Westernblot. PC-3M-Pro4 containing SCR, ITGB1 kd1 , ILK kd1 CDC42 kd1 and N-Wasp kd1 were seed for monolayer culture. Protein samples were harvested at 48 hours after seeding. (g) QPCR analysis of CRY61 expression. Experiments were independently repeated 2 times. *p<0.05, **p<0.01, ***p<0.001, ****p<0,0001. Arrow bars are s.e.m.

TAZ controls CSC-like phenotypes *in vitro* and metastatic tumor initiation *in vivo*

We next investigated if the integrin β1-ILK-CDC42-N-Wasp axis controls PCa metastasis initiation through TAZ activation. To monitor the subcellular localization of TAZ during metastasis initiation, TAZ-GFP was ectopically expressed in the PC-3M-Pro4-Lifeact-mcherry cells. Before transplantation, the cells were cultured at a high confluence (>90%) to block TAZ nuclear translocation by inducing Hippo signaling [46] (Fig. 7a). Directly after transplantation, TAZ-GFP was retained in the cytoplasm in the rounded circulating cancer cells (Fig. 7b). When the metastases was initiated at 4 dpi, TAZ was activated and translocated into nucleus in the spreading cancer cells at the metastatic site (Fig. 7b). We next generated YAP and TAZ knockdown cells. This YAP and TAZ knockdowns significantly inhibited expression of pluripotency genes NANOG, OCT4 and BMI1 (Fig. 7c, Fig. S3d). Since TAZ (but not YAP) is highly expressed in patients' metastases and both TAZ knockdowns displayed stronger inhibitory effects on pluripotency gene expression than the YAP knockdowns (Fig. 1a, 1b, 7c and S3d), we further checked the effects of the TAZ knockdowns on CSC-like phenotypes and metastasis. Tumorspheroid formation from single cell in MoT 3D culture and clonogenicity were both significantly inhibited by both TAZ knockdowns (Fig. 7e). *In vivo*, both TAZ knockdowns significantly suppressed metastatic outgrowth at 4 and 6 dpi. To further confirm if the TAZ knockdowns inhibited the cancer cell proliferation at metastatic onset, whole mount immunostaining was performed to determine cell proliferation. As expected Ki-67 signal was reduced in the TAZ kd cells (Fig. 7f).

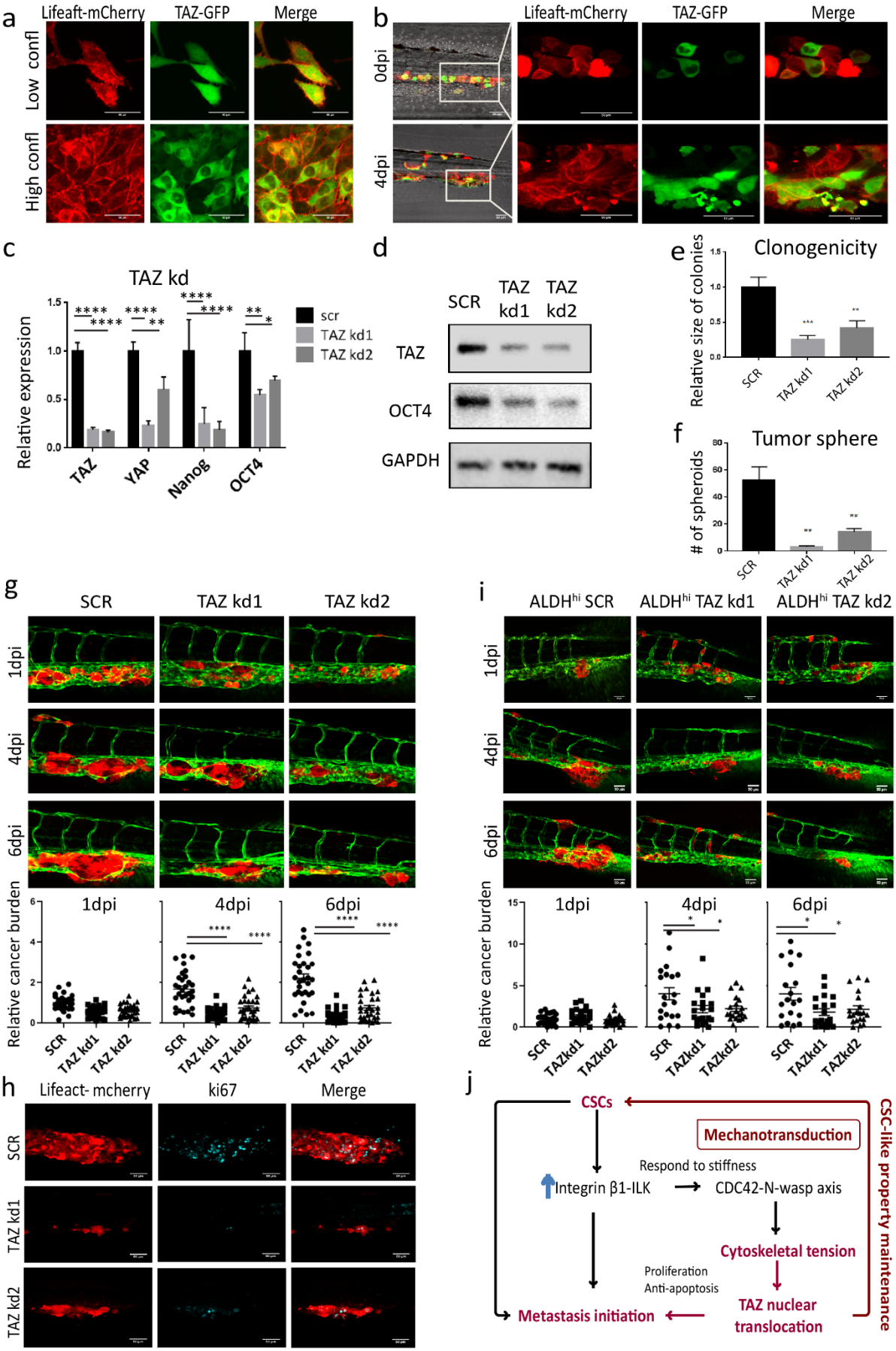
a
Lifeaft-mCherry
TAZ-GFP
Merge
Low confl
High confl
b
Lifeaft-mCherry
TAZ-GFP
Merge
0dpi
4dpi
c
TAZ kd
Relative expression
scr
TAZ kd1
TAZ kd2
TAZ
YAP
Nanog
OCT4
d
SCR
TAZ kd1
TAZ kd2
TAZ
OCT4
GAPDH
e
Clonogenicity
Relative size of colonies
SCR
TAZ kd1
TAZ kd2
f
Tumor sphere
# of spheroids
SCR
TAZ kd1
TAZ kd2
g
SCR
TAZ kd1
TAZ kd2
1dpi
4dpi
6dpi
Relative cancer burden
1dpi
4dpi
6dpi
SCR
TAZ kd1
TAZ kd2
i
ALDHhi SCR
ALDHhi TAZ kd1
ALDHhi TAZ kd2
1dpi
4dpi
6dpi
Relative cancer burden
1dpi
4dpi
6dpi
SCR
TAZkd1
TAZkd2
h
Lifeact- mcherry
ki67
Merge
SCR
TAZ kd1
TAZ kd2
j
CSCs
Mechanotransduction
Respond to stiffness
Integrin β1-ILK
CDC42-N-wasp axis
Cytoskeletal tension
Proliferation
Anti-apoptosis
TAZ nuclear translocation
Metastasis initiation
CSC-like property maintenance

Fig. 7 PCa CSC-like properties and metastasis initiation are inhibited by YAP/TAZ knockdowns. (a) Subcellular localization of TAZ-GFP in PC-3M-Pro4 at low or high confluence in 2D culture. Scare bar = 50um. (b) Subcellular localization of TAZ-GFP in PC-3M-Pro4 in ZF xenografts. PC-3M-Pro4-Lifeact-mCheery-TAZ-GFP was injected into ZF. Confocal images were acquired at 3hpi and 4dpi. Scare bar = 50um. (c) Effects of TAZ knockdowns on the expression of pluripotency genes. Experiments were independently repeated 2 times. (d) Effects of TAZ knockdowns on the protein level of OCT4. (e) Effects of TAZ knockdowns on cell clonogenicity (e) and tumor spheroid formation (f). Each experiment was independently repeated 3 times. (f) Effects of TAZ knockdowns on the metastatic outgrowth of PCa cells. PC-3M-Pro4-Lifeact-mCherry containing SCR, TAZ kd1 and TAZ kd2 were respectively injected into ZF. Total cancer cell burden at metastatic site was measured at 1, 4, 6 dpi. Up, representative images of the metastases. Scare bar = 50um. Down, quantification. Group size = 30. (g) Immunofluorescence against Ki-67 was performed on the ZF metastatic site at 6dpi. Scare bar = 50um. The ratio of the fluorescent signal between Ki-67 and Lifeact-mCherry was calculated using Image-J. (h) $ALDH^{hi}$ subpopulation was isolated from PC-3M-Pro4-Lifeact-mCherry containing SCR, TAZ kd1 and TAZ kd2 and injected into ZF. Total cancer cell burden at metastatic site was measured at 1, 4, 6 dpi. up, representative images of the metastases. Scare bar = 50um. Down, quantification. Group size = 20. *p<0.05, **p<0.01, ***p<0.001, ****p<0,0001. Arrow bars are s.e.m. (i) Schematic representation of the proposed role of integrin-dependent mechanotransduction in driving PCa metastasis. At metastatic onset, Integrin-β1 and ILK, which are highly expressed in CSC-LCs, mediate mechanotransduction through CDC42-N-Wasp dependent actin dynamics inducing YAP/TAZ nuclear translocation when the cells respond to the stiffness. This YAP/TAZ nuclear translocation promotes stemness gene expression triggering metastatic tumorigenicity. Although TAZ kd did not significantly change the percentage of the $ALDH^{hi}$ subpopulation, injection of $ALDH^{hi}$ cells containing TAZ knockdowns in ZF at 4 and 6 dpi, showed significant suppression of the metastatic tumor outgrowth, indicating that TAZ activation drives metastatic capacity of the $ALDH^{hi}$ cells (Fig. 7h).

Pharmacological targeting of integrin-TAZ axis inhibits PCa cell proliferation *in vitro*

We next assessed if pharmacological inhibition of the Integrin-YAP/TAZ axis could be a potential approach to suppress PCa cell growth. Therefore PC-3, PC-3M-Pro4 and C4-2B were respectively treated with integrin α2β1 inhibitor BTT 3033, ILK inhibitor CPD22 and YAP/TAZ inhibitor Verteporfin [47-49]. All of the treatments significantly suppressed the cell growth in monolayer culture after 72hours of exposure (Fig. S7a-S7c).

Pharmacological targeting integrin-TAZ axis inhibits Organoids formation and growth

To further test the clinical potential of targeting integrin-TAZ axis, we assessed YAP/TAZ and the downstream genes CTGF, AMTOL2 and CYR61 expression in the patient derived xenograft LAPC9 (craft). Only YAP was not detectable (Fig. 8a). Immunofluorescence of LAPC9 organoids showed p-Paxillin co-localized with F-actin at the cell edge, indicating the formation of focal adhesion plaques (Fig. 8c). TAZ nuclear expression was also detected in few cells at the peripheral cell layer (Fig. 8c).

We next treated the LAPC9 organoids with BTT 3033, CPD22 and Verteporfin at 72 hours after seeding. Viability was significantly reduced in a dose dependent manner by all inhibitors (Fig. 8d), suggesting integrin-TAZ axis is indispensable for PCa organoids development and the pharmacological targeting of this cascades may have a clinical value.

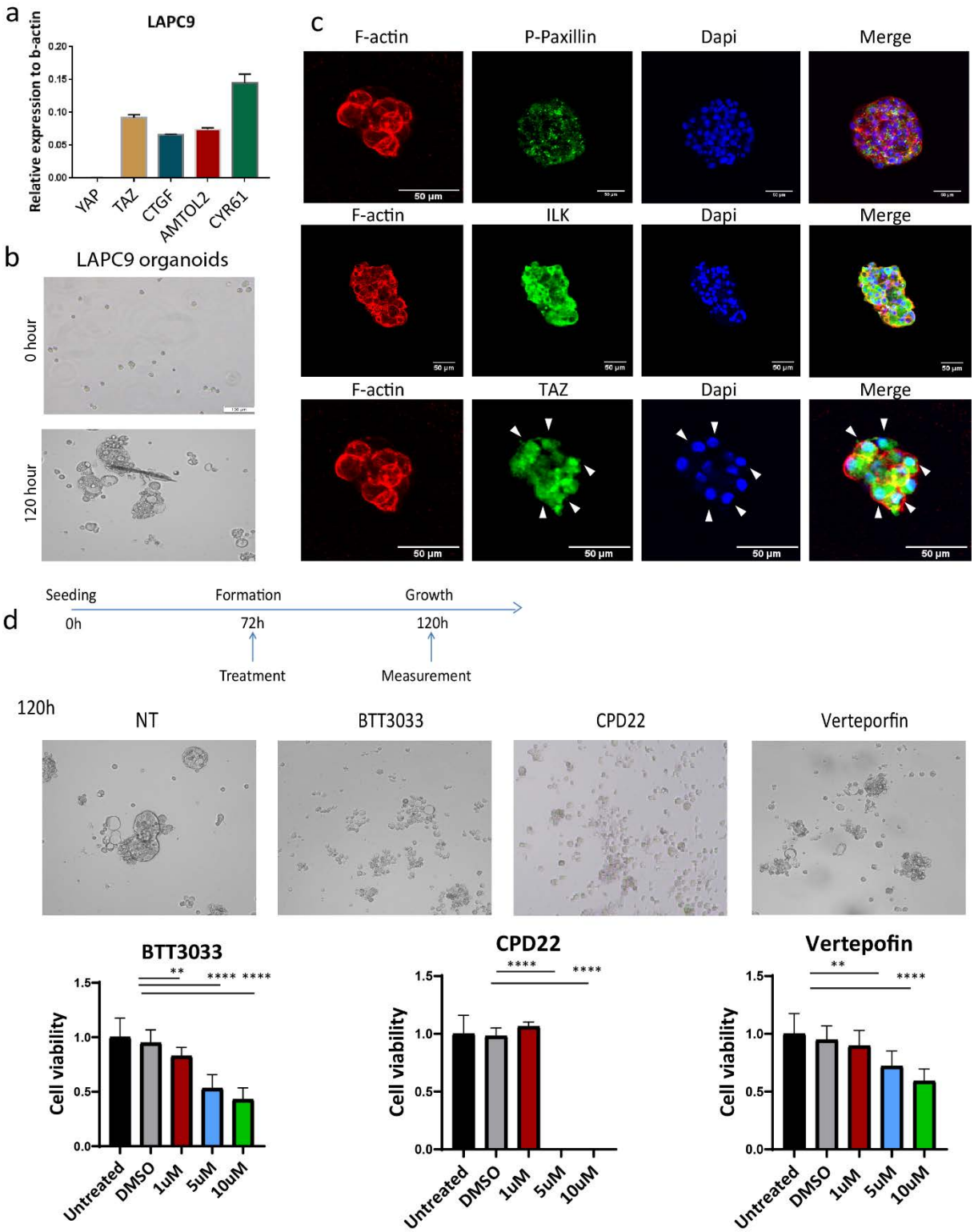

Fig. 8 Pharmacological inhibition of integrin β1, ILK and YAP/TAZ suppresses growth of PCa organoids. (a) Expression of YAP/TAZ and their downstream genes in LAPC9 PDX tissue. (b) Representative images of LAPC9 organoids development. (c) Subcellular localization of p-Paxillin, ILK and TAZ in LAPC9 organoids. Immunofluorescence was performed at 120 hours after seeding. Scare bar = 50um. (d) Effects of integrin α2β1 inhibitor BTT3033, ILK inhibitor CPD22 and YAP/TAZ inhibitor Verteporfin on the growth of LAPC9 organoids. The organoids were exposed to the inhibitors at 72h after seeding. Cell viability was measured at 48 hour after treatments. Experiments were independently repeated 2 times. Group size = 8. *p<0.05, **p<0.01, ***p<0.001, ****p<0,0001. Arrow bars are s.e.m.

Discussion

In prostate cancer (PCa), there is a critical need to understand the features of the heterogenic subpopulation of cells that are associated with progression to lethal bone metastasis. Considering that PCa patient-derived cancer stem-cells (CSCs) have elevated expression of cell adhesion, and of the mechano-regulator TAZ [26, 27, 50], we here investigated the correlation between CSC-LCs mechanotransduction and their metastatic behavior.

Our data show that the aggressive CSC-like phenotype of PCa cells relies critically on their enhanced mechanosensing and mechanotransduction potential. Combining measurements of mechano-responses to matrix stiffness, analysis of the respective cellular forces, zebrafish and mice xenografts, and PDX-derived organoids, we demonstrated that PCa CSC-LCs have an enhanced response to the mechanical cues through upregulated expression of integrin β1 and ILK. This integrin-dependent mechanical response in turn leads to CDC42-N-Wasp associated cytoskeleton remodeling and nuclear translocation of TAZ, which ultimately promotes the stemness character of the cells and leads to initiation of metastatic outgrowth (Fig. 7i).

The therapeutic potential for targeting this integrin-ILK-YAP/TAZ pathway we assessed using PCa organoids. During the formation and growth of LAPC9 organoids, TAZ was activated at the peripheral cell layer accompanied by the formation of focal adhesion plaques, and by elevated ILK expression (Fig. 8c). Targeting of this integrin-TAZ axis by an inhibitor of integrin α2β1, an ILK inhibitor, and a YAP/TAZ inhibitor significantly attenuated the formation and growth of these organoids (Fig. 8d). Our results are consistent with previous studies of intestinal organoids, which showed that the mechanical signal from the matrix governs intestinal stem cell proliferation and therefore organoid formation through regulating YAP/TAZ activity [51, 52].

Integrin-dependent cytoskeleton dynamics has been reported to control metastatic outgrowth [11, 40]. Shibue et al found that the formation and extension of filopodia-like protrusions (FLPs) is driven by Rif-mDIA2 and by ILK-LIMK1-coffilin signaling pathways. Both are key steps of tumor initiation and metastatic colonization in melanoma and breast cancer [11, 40]. Consistently, our study showed that ILK-dependent FLPs were increasingly formed in the $ALDH^{hi}$ CSC enriched cell population in MoT 3D culture (Fig. 2f). Although the formation of FLPs is significantly suppressed in integrin β1 and ILK knockdown cells in MoT culture, substantial FLPs were still formed in ITGB1 kd and ILK kd cells *in vivo* (Fig. 4c). In addition, proliferation of ITGB1 kd and ILK kd cells was significantly reduced *in vivo* accompanied by an impaired cell elongation. Together our data suggest that additional integrin-dependent actin factors were involved in the regulation of metastatic outgrowth. Indeed, our *in vivo* shRNA screening showed that knockdown of the lamellipodia/invadopodia components N-Wasp and cortactin, rather than knockdown of the FLP component mDIA2, gave the strongest inhibitory effect on metastatic tumor outgrowth. Invadopodia are defined as actin-enriched protrusion facilitating cancer-cell extravasation and invasion. Yet, its role in metastatic outgrowth of cancer has been less well documented [53-56]. Using a Fucci-based reporter, we found that

knockdown of N-Wasp and its upstream CDC42 significantly attenuated cancer-cell proliferation at metastatic onset in zebrafish xenografts. This result indicates that the invadopodia components contribute to cancer-cell outgrowth during metastasis [45]. We further demonstrated that the CDC42-N-Wasp-dependent cytoskeleton remolding controls cancer stem-like phenotype and metastatic tumor outgrowth, at least partially, by mechanotransduction and YAP/TAZ activation.

YAP/TAZ activation is regulated by two distinguishing mechanisms: the Hippo signaling pathway, and a mechano-related cytoskeletal reorganization and stiffening process [18]. Isabel et al suggested that ILK promoted YAP/TAZ nuclear translocation by regulating Hippo signaling through the suppression of the Hippo phosphorylation Merlin-MST1/2-LATS1/2-YAP/TAZ axis [57]. However, our study showed that both ILK and its upstream integrin β1 regulate YAP/TAZ activity in a Hippo-independent manner. This conclusion we derived from our observation that integrin β1 and ILK knockdown did not affect the phosphorylation of MST1, LATS1/2 or YAP/TAZ (Fig. 6f). We hence propose that regulation of YAP/TAZ by integrin was mainly driven by mechano-related cytoskeletal reorganization processes. In line with our proposal was the observation that knockdown of either integrin β1, ILK, CDC42 or N-Wasp significantly attenuated both cellular contractility and YAP/TAZ nuclear translocation, yet without affecting components of the Hippo pathway. Notably, the total protein level of YAP was suppressed by knockdown of either integrin β1, ILK or CDC42. This result is concordant with a previous study, which showed that mechano-factors and actin polymerization control both total protein level and subcellular localization of YAP in a hippo-independent manner [18].

In conclusion, our study shows that PCa CSC-like cells critically respond to external stiffness and generate intrinsic forces that further enhance their pathological metastasis into stiff tissue like bone. We further presented experimental evidence that targeting of this process inhibited metastasis in zebrafish and mice xenografts and effected tumor growth of near-patient organoids. Hence our study highlights the eminent role of integrin-dependent mechanotransduction in PCa metastasis initiation, which should encourage investigation of the pathway as therapeutic target in the future.

Acknowledgments

We thank Dr. Gabriel van der Pluijm (Deportment of Urology, LUMC) for providing experimental material. Guido de Roo from the Flow cytometry facility (Department of Hematology, LUMC) for technical support, Martijn Rabelink and Prof. Rob Hoeben (Department of Cell Biology, LUMC) for providing lenti-viral shRNA vectors (Sigma-Aldrich). The present work was supported by a personalized medicine grant from Alpe D'HuZes (AdH)/KWF PROPER entitled “Near-patient prostate cancer models for the assessment of disease prognosis and therapy” (UL2014-7058).

References

1. Jemal, A., et al., *Global patterns of cancer incidence and mortality rates and trends.* Cancer Epidemiol Biomarkers Prev, 2010. **19**(8): p. 1893-907.
2. Collins, A.T., et al., *Prospective identification of tumorigenic prostate cancer stem cells.* Cancer Res, 2005. **65**(23): p. 10946-51.
3. Shiozawa, Y., et al., *Human prostate cancer metastases target the hematopoietic stem cell niche to establish footholds in mouse bone marrow.* Journal of Clinical Investigation, 2011. **121**(4): p. 1298-1312.
4. Shiozawa, Y., et al., *The marrow niche controls the cancer stem cell phenotype of disseminated prostate cancer (vol 7, pg 41217, 2016).* Oncotarget, 2017. **8**(23): p. 38075-38075.
5. Lambert, A.W., D.R. Pattabiraman, and R.A. Weinberg, *Emerging Biological Principles of Metastasis.* Cell, 2017. **168**(4): p. 670-691.
6. Birnie, R., et al., *Gene expression profiling of human prostate cancer stem cells reveals a pro-inflammatory phenotype and the importance of extracellular matrix interactions.* Genome Biol, 2008. **9**(5): p. R83.
7. Ghotra, V.P., et al., *SYK is a candidate kinase target for the treatment of advanced prostate cancer.* Cancer Res, 2015. **75**(1): p. 230-40.
8. Parsons, J.T., A.R. Horwitz, and M.A. Schwartz, *Cell adhesion: integrating cytoskeletal dynamics and cellular tension.* Nat Rev Mol Cell Biol, 2010. **11**(9): p. 633-43.
9. Clark, E.A., et al., *Integrin-mediated signals regulated by members of the rho family of GTPases.* J Cell Biol, 1998. **142**(2): p. 573-86.
10. Eddy, R.J., et al., *Tumor Cell Invadopodia: Invasive Protrusions that Orchestrate Metastasis.* Trends Cell Biol, 2017. **27**(8): p. 595-607.
11. Shibue, T., M.W. Brooks, and R.A. Weinberg, *An integrin-linked machinery of cytoskeletal regulation that enables experimental tumor initiation and metastatic colonization.* Cancer Cell, 2013. **24**(4): p. 481-98.
12. Goodman, M.B., et al., *Molecules and mechanisms of mechanotransduction.* J Neurosci, 2004. **24**(42): p. 9220-2.
13. Orr, A.W., et al., *Mechanisms of mechanotransduction.* Dev Cell, 2006. **10**(1): p. 11-20.
14. Salvi, A.M. and K.A. DeMali, *Mechanisms linking mechanotransduction and cell metabolism.* Curr Opin Cell Biol, 2018. **54**: p. 114-120.
15. Dupont, S., et al., *Role of YAP/TAZ in mechanotransduction.* Nature, 2011. **474**(7350): p. 179-83.
16. Dupont, S., *Role of YAP/TAZ in cell-matrix adhesion-mediated signalling and mechanotransduction.* Exp Cell Res, 2016. **343**(1): p. 42-53.
17. Malakou, L.S., et al., *Molecular mechanisms of mechanotransduction in psoriasis.* Ann Transl Med, 2018. **6**(12): p. 245.
18. Aragona, M., et al., *A mechanical checkpoint controls multicellular growth through YAP/TAZ regulation by actin-processing factors.* Cell, 2013. **154**(5): p. 1047-1059.
19. Mohri, Z., A. Del Rio Hernandez, and R. Krams, *The emerging role of YAP/TAZ in mechanotransduction.* J Thorac Dis, 2017. **9**(5): p. E507-E509.
20. Yui, S., et al., *YAP/TAZ-Dependent Reprogramming of Colonic Epithelium Links ECM Remodeling to Tissue Regeneration.* Cell Stem Cell, 2018. **22**(1): p. 35-49 e7.
21. Han, D., et al., *YAP/TAZ enhance mammalian embryonic neural stem cell characteristics in a Tead-dependent manner.* Biochem Biophys Res Commun, 2015. **458**(1): p. 110-6.
22. Tang, Y., et al., *Snail/Slug binding interactions with YAP/TAZ control skeletal stem cell self-renewal and differentiation.* Nat Cell Biol, 2016. **18**(9): p. 917-29.
23. Ohgushi, M., M. Minaguchi, and Y. Sasai, *Rho-Signaling-Directed YAP/TAZ Activity Underlies the Long-Term Survival and Expansion of Human Embryonic Stem Cells.* Cell Stem Cell, 2015. **17**(4): p. 448-61.

24. Panciera, T., et al., *Induction of Expandable Tissue-Specific Stem/Progenitor Cells through Transient Expression of YAP/TAZ.* Cell Stem Cell, 2016. **19**(6): p. 725-737.
25. Imajo, M., M. Ebisuya, and E. Nishida, *Dual role of YAP and TAZ in renewal of the intestinal epithelium.* Nature Cell Biology, 2015. **17**(1): p. 7-+.
26. Zanconato, F., M. Cordenonsi, and S. Piccolo, *YAP/TAZ at the Roots of Cancer.* Cancer Cell, 2016. **29**(6): p. 783-803.
27. Cordenonsi, M., et al., *The Hippo transducer TAZ confers cancer stem cell-related traits on breast cancer cells.* Cell, 2011. **147**(4): p. 759-72.
28. Li, Y.W., et al., *Apigenin suppresses the stem cell-like properties of triple-negative breast cancer cells by inhibiting YAP/TAZ activity.* Cell Death Discov, 2018. **4**: p. 105.
29. van Hoorn, H., et al., *The nanoscale architecture of force-bearing focal adhesions.* Nano Lett, 2014. **14**(8): p. 4257-62.
30. Ghibaudo, M., et al., *Traction forces and rigidity sensing regulate cell functions.* Soft Matter, 2008. **4**(9): p. 1836-1843.
31. Zack, G.W., W.E. Rogers, and S.A. Latt, *Automatic measurement of sister chromatid exchange frequency.* J Histochem Cytochem, 1977. **25**(7): p. 741-53.
32. Lawson, N.D. and B.M. Weinstein, *In vivo imaging of embryonic vascular development using transgenic zebrafish.* Dev Biol, 2002. **248**(2): p. 307-18.
33. He, S., et al., *Neutrophil-mediated experimental metastasis is enhanced by VEGFR inhibition in a zebrafish xenograft model.* J Pathol, 2012. **227**(4): p. 431-45.
34. Chen, L., et al., *A zebrafish xenograft model for studying human cancer stem cells in distant metastasis and therapy response.* Methods Cell Biol, 2017. **138**: p. 471-496.
35. Tulotta, C., et al., *Imaging of Human Cancer Cell Proliferation, Invasion, and Micrometastasis in a Zebrafish Xenogeneic Engraftment Model.* Methods Mol Biol, 2016. **1451**: p. 155-69.
36. Taylor, B.S., et al., *Integrative genomic profiling of human prostate cancer.* Cancer Cell, 2010. **18**(1): p. 11-22.
37. Grasso, C.S., et al., *The mutational landscape of lethal castration-resistant prostate cancer.* Nature, 2012. **487**(7406): p. 239-43.
38. Ishihara, E. and H. Nishina, *[Role of Hippo-YAP/TAZ signaling pathway in mechanotransduction.].* Clin Calcium, 2016. **26**(12): p. 1751-1756.
39. van den Hoogen, C., et al., *High aldehyde dehydrogenase activity identifies tumor-initiating and metastasis-initiating cells in human prostate cancer.* Cancer Res, 2010. **70**(12): p. 5163-73.
40. Shibue, T., et al., *The outgrowth of micrometastases is enabled by the formation of filopodium-like protrusions.* Cancer Discov, 2012. **2**(8): p. 706-21.
41. Riedl, J., et al., *Lifeact: a versatile marker to visualize F-actin.* Nat Methods, 2008. **5**(7): p. 605-7.
42. Turner, C.E., *Paxillin and focal adhesion signalling.* Nat Cell Biol, 2000. **2**(12): p. E231-6.
43. Wu, C. and S. Dedhar, *Integrin-linked kinase (ILK) and its interactors: a new paradigm for the coupling of extracellular matrix to actin cytoskeleton and signaling complexes.* J Cell Biol, 2001. **155**(4): p. 505-10.
44. Dai, J., et al., *Mouse models for studying prostate cancer bone metastasis.* Bonekey Rep, 2016. **5**: p. 777.
45. Zielke, N. and B.A. Edgar, *FUCCI sensors: powerful new tools for analysis of cell proliferation.* Wiley Interdiscip Rev Dev Biol, 2015. **4**(5): p. 469-87.
46. Piccolo, S., S. Dupont, and M. Cordenonsi, *The biology of YAP/TAZ: hippo signaling and beyond.* Physiol Rev, 2014. **94**(4): p. 1287-312.
47. Nissinen, L., et al., *Novel alpha2beta1 integrin inhibitors reveal that integrin binding to collagen under shear stress conditions does not require receptor preactivation.* J Biol Chem, 2012. **287**(53): p. 44694-702.
48. Lee, S.L., et al., *Identification and characterization of a novel integrin-linked kinase inhibitor.* J Med Chem, 2011. **54**(18): p. 6364-74.

49. Liu-Chittenden, Y., et al., *Genetic and pharmacological disruption of the TEAD-YAP complex suppresses the oncogenic activity of YAP.* Genes Dev, 2012. **26**(12): p. 1300-5.
50. Liu, N., et al., *Phosphodiesterase 5/protein kinase G signal governs stemness of prostate cancer stem cells through Hippo pathway.* Cancer Lett, 2016. **378**(1): p. 38-50.
51. Gregorieff, A., et al., *Yap-dependent reprogramming of Lgr5(+) stem cells drives intestinal regeneration and cancer.* Nature, 2015. **526**(7575): p. 715-718.
52. Glorevski, N., et al., *Designer matrices for intestinal stem cell and organoid culture.* Nature, 2016. **539**(7630): p. 560-+.
53. Liu, J., et al., *The role of the exocyst in matrix metalloproteinase secretion and actin dynamics during tumor cell invadopodia formation.* Mol Biol Cell, 2009. **20**(16): p. 3763-71.
54. Buccione, R., G. Caldieri, and I. Ayala, *Invadopodia: specialized tumor cell structures for the focal degradation of the extracellular matrix.* Cancer Metastasis Rev, 2009. **28**(1-2): p. 137-49.
55. Leong, H.S., et al., *Invadopodia are required for cancer cell extravasation and are a therapeutic target for metastasis.* Cell Rep, 2014. **8**(5): p. 1558-70.
56. Markwell, S.M., et al., *Cortactin Phosphorylation by Casein Kinase 2 Regulates Actin-Related Protein 2/3 Complex Activity, Invadopodia Function and Tumor Cell Invasion.* Mol Cancer Res, 2019.
57. Serrano, I., et al., *Inactivation of the Hippo tumour suppressor pathway by integrin-linked kinase.* Nat Commun, 2013. **4**: p. 2976.

Supplementary Figures

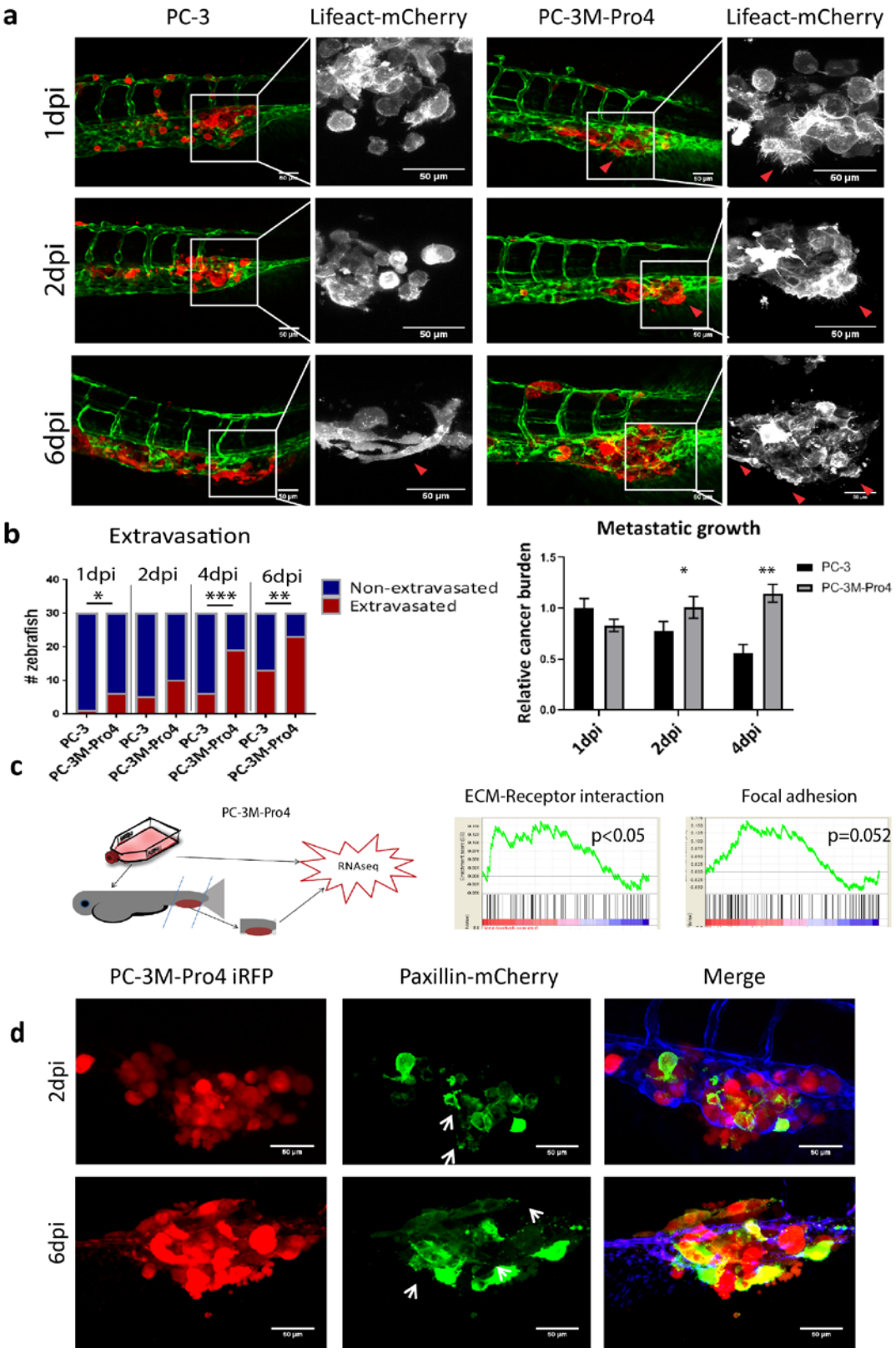

Fig. S1 Metastatic onset of PCa cells is associated with focal adhesion and cytoskeleton dynamics. (a) PC-3-Lifeact-mCherry and PC-3M-Pro4-Lifeact-mCherry were respectively injected into ZF vasculature. Metastasis at

CHT was imaged using confocal at 1, 2 and 6dpi. Green, ZF vasculature; red, cancer cells; Gray, Enlargement of the cancer cells. Arrow, actin protrusions. (b) Extravasation and total cancer cell burden were measured at 1, 2, 4 dpi. Scale bar = 50um. Group size = 30. (c) Transcriptomics of PC-3M-Pro4 was compared between in ZF metastases and in culture. Result was analyzed with Gene Set Enrichment Analysis (GSEA). (d) PC-3M-Pro4-iRFP (red) was transduced with Paxillin-mCheery (green). After injection, subcellular localization of Paxillin-mCherry was detected at 2 and 6 dpi using confocal. Scale bar = 50um. Arrow, focal adhesion plaques.

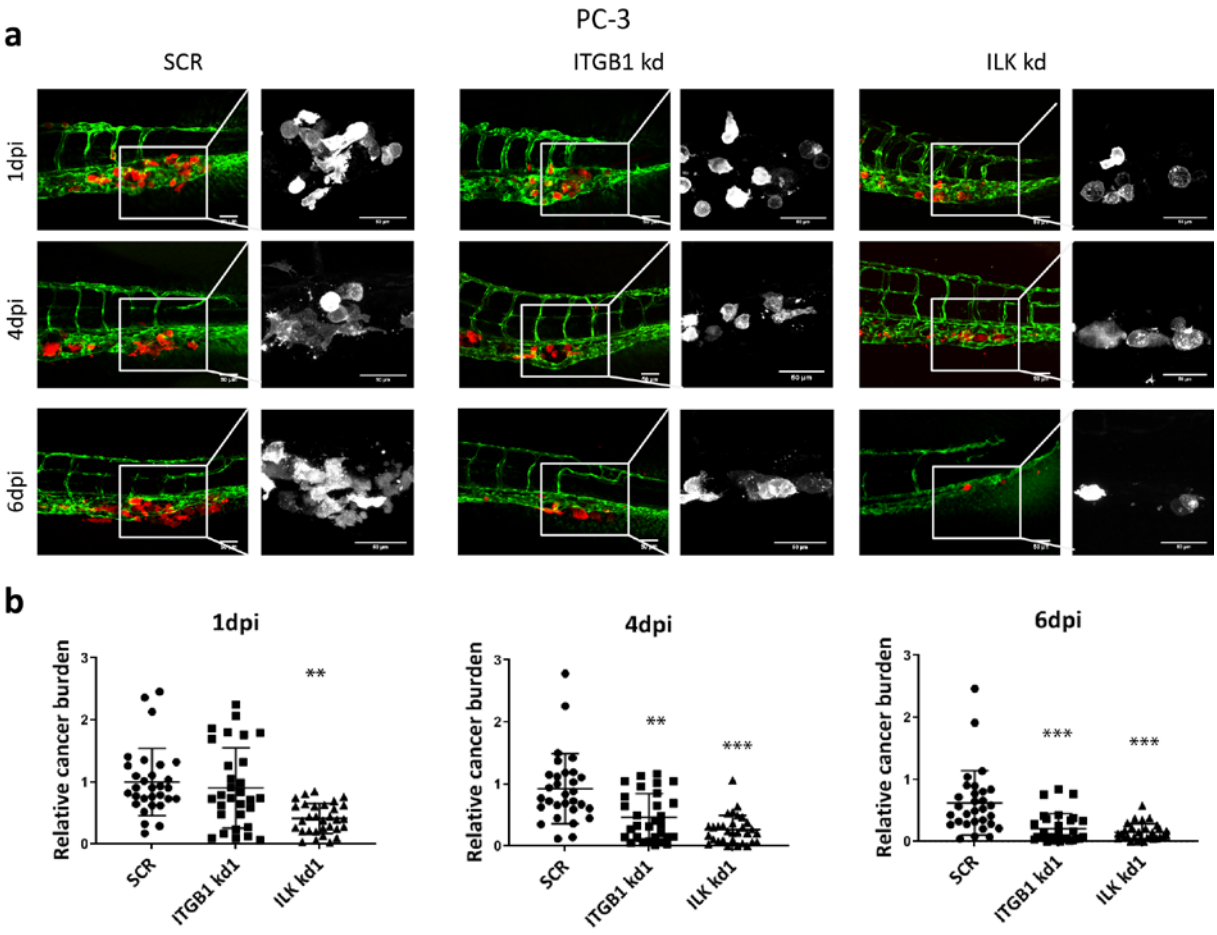

Fig. S2 Knockdown of Integrin β1 and ILK inhibits metastatic onset of PC-3. (a) PC-3-Lifeact-mCherry-SCR, ITGB1 kd1 and ILK kd1 were injected into ZF. Confocal images were acquired at 1, 4 and 6 dpi. Scale bar = 50uM. (b)Analysis of total cancer cell burden at 1, 4 and 6 dpi at metastatic site. Intensity of mCherry fluorescence was measured using ZF4 pixel counter program. (n=30).

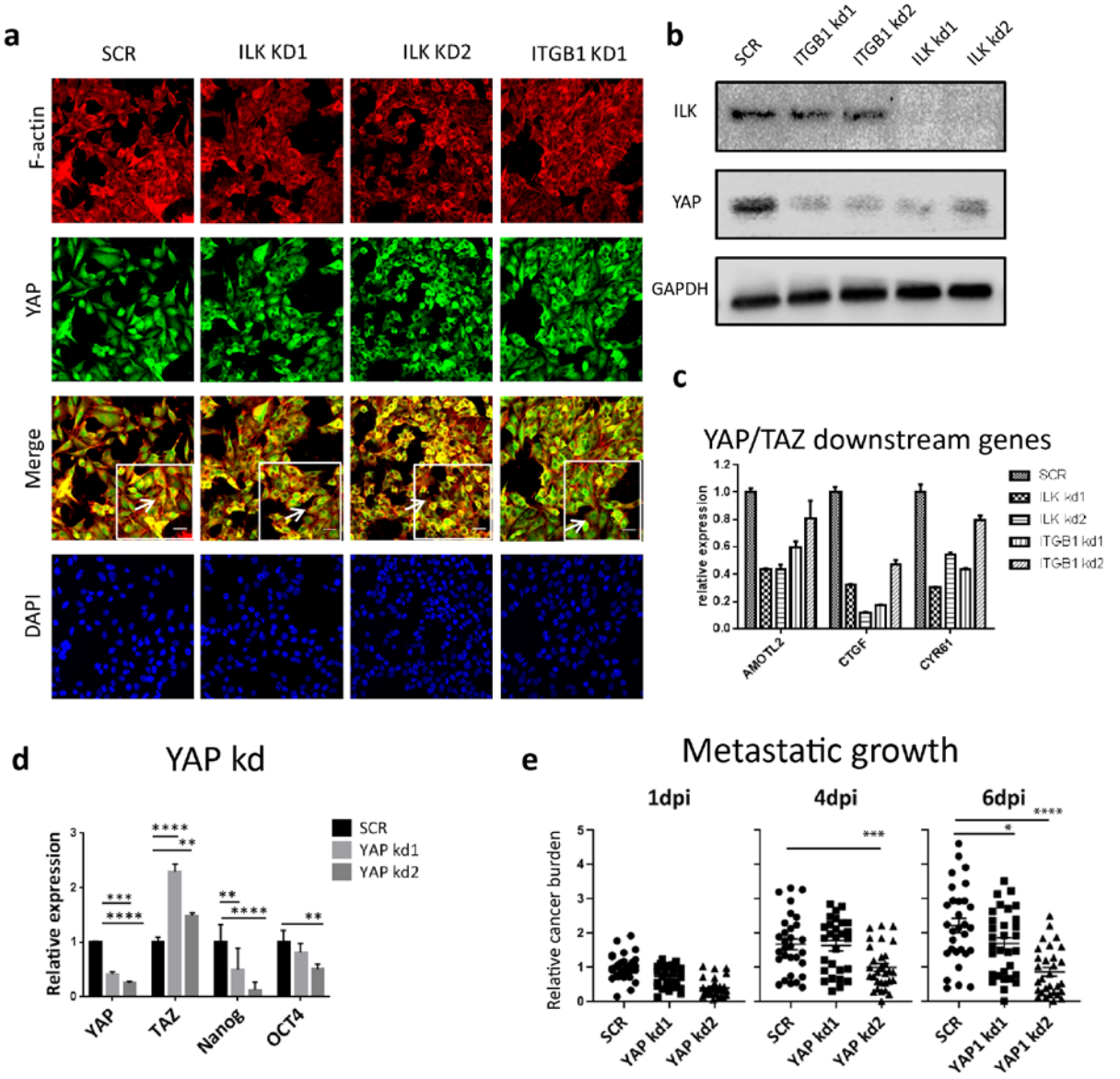

Fig. S3 YAP is regulated by integrin β1 and ILK and is required for pluripotency gene expression and metastatic onset. (a) PC-3M-Pro4 was cultured as monolayer on glass. Immunostaining was performed against YAP. Red, F-actin; Green, YAP; Blue, Dapi. (b) Total protein level of YAP was measured in PC-3M-Pro4-SCR,- ITGB1 kd and –ILK kd using westernblot. (c) Expression of AMTOL2, CTGF and CYR61 was measured by qPCR. (d) Effects of YAP knockdowns on pluripotency gene expression. (e) PC-3M-Pro4-Lifeact-mCherry containing either SCR control, YAP kd1 or YAP kd2 were respectively injected into ZF. Total cancer burden at CHT area was measured at 1, 4 and 6 dpi. Group size = 30

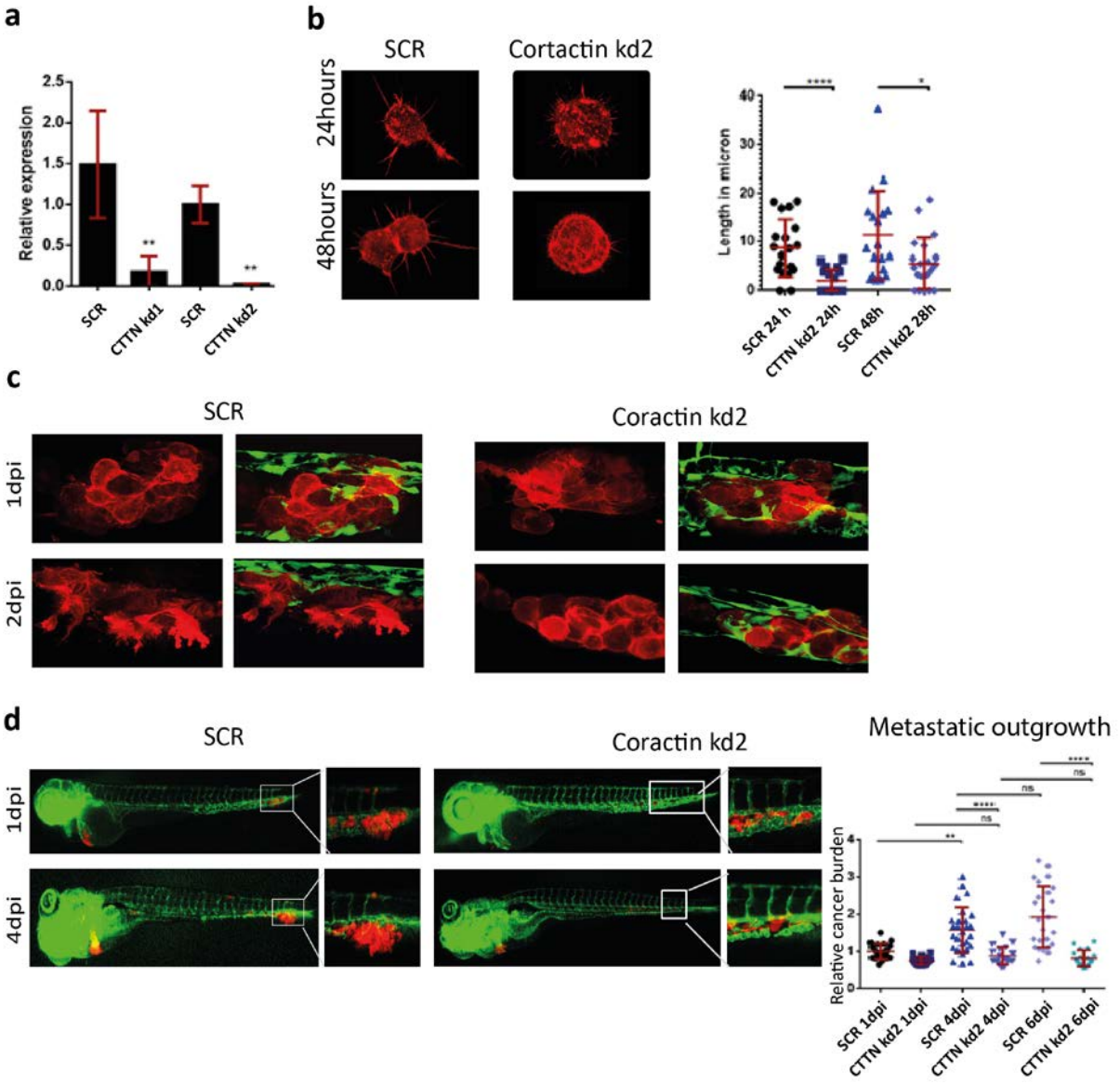

Fig. S4 Knockdown of Cortactin inhibits actin polymerization and metastatic onset. (a) Validation of Cortactin (CTTN) knockdown in PC-3M-Pro4 using qPCR. (b) Effects of Cortactin knockdown on FLPs formation on MOT culture. Images were acquired at 24 and 48 hours after seeding. Total length of FLPs was counted using Image J. Group size = 15. (c) PC-3M-Pro4-Lifeact-mCherry-SCR and –CTTN kd2 were injected into ZF. Actin dynamics of the cancer cells were imaged at 1 and 2 dpi. (d) Total cancer cell burden at CHT was measured using ZF4 pixel counter. Group size = 30.

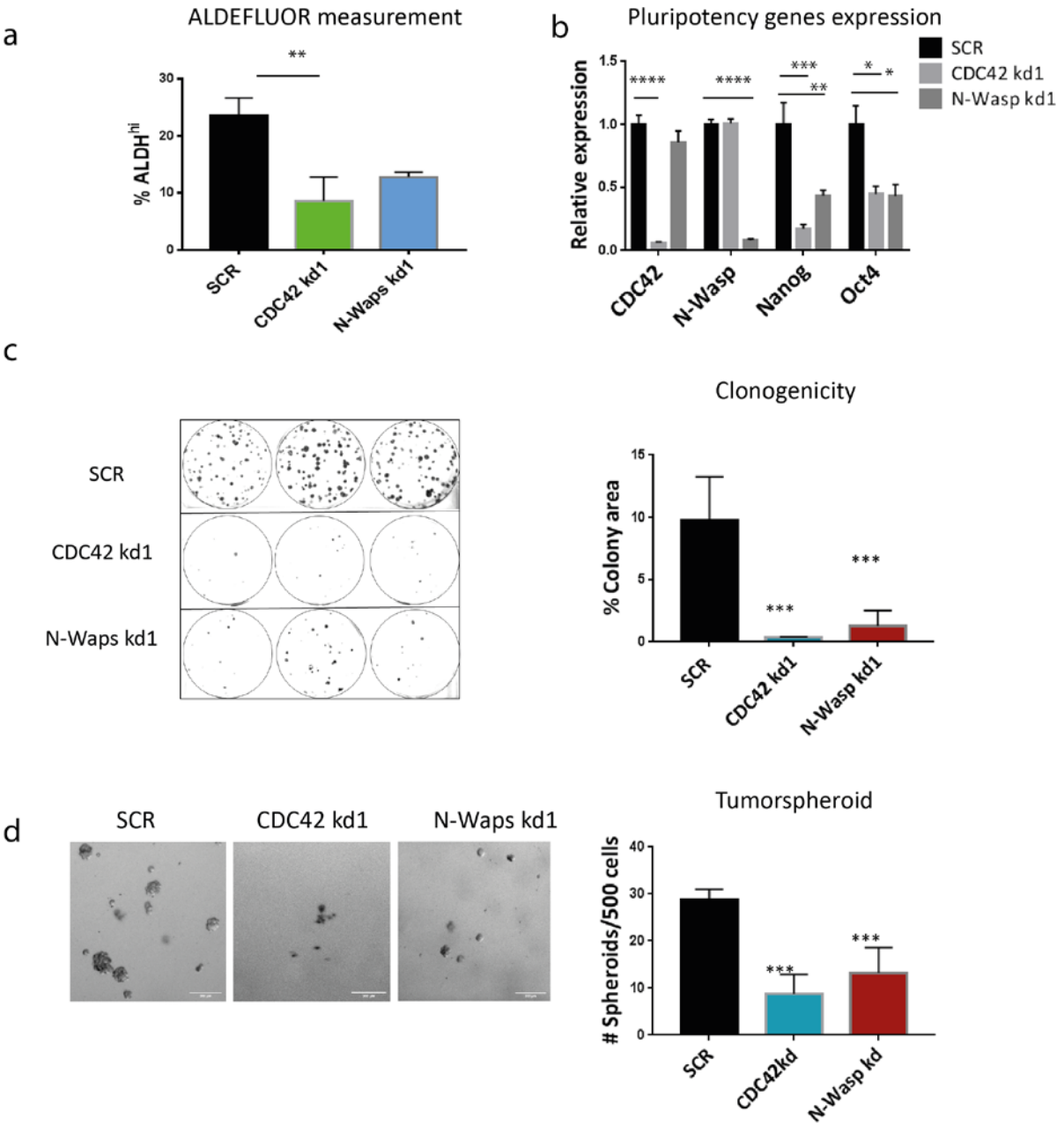

Fig. S5 Knockdown of CDC42 and N-Wasp inhibits CSC-like properties. (a) Size of ALDH^{hi} was compared between PC-3M-Pro4-SCR, -CDC42 kd1 and -N-Wasp kd1. Experiments were independently repeated twice. (b) Expression of CDC42, N-Wasp, NANOG and OCT4 was compared between PC-3M-Pro4-SCR, -CDC42 kd1 and -N-Wasp kd1 when the cells were growing in MOT 3D culture for 96 hours. Experiments were independently repeated twice. (c-d) Effects of CDC42 and N-Wasp knockdowns on clonogenicity and tumorspheroid formation. 500 cells/well were seed. Data was acquired at 14 days after seeding. Total colony area was measured using Image-J. Experiments were repeated 2 times.

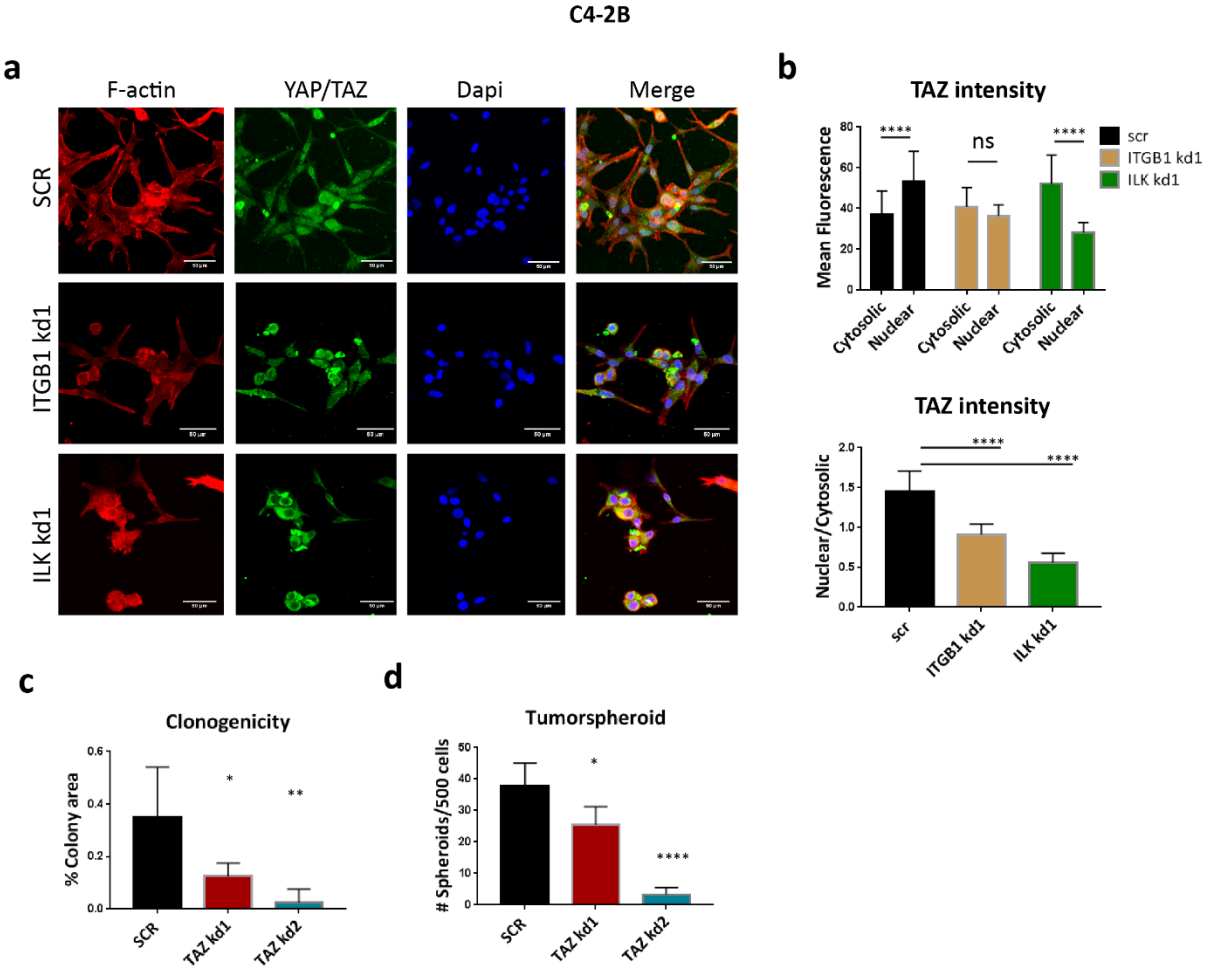

Fig. S6 Knockdown of TAZ inhibits cell clonogenicity and tumor spheroid in C4-2B. (a) Effect of Integrin β1 and ILK knockdown on YAP/TAZ nuclear translocation of C4-2B on 2D culture. Cells were cultured for 48 hours. Immunofluorescence was performed against YAP/TAZ. Large bar = 50um. (b) YAP/TAZ cyotosolic/nuclear intensity was measure using Image-J. 15 cells from 2 independent experiments were analyzed. (c) Effects of ITAZ knockdown on clonogenicity of C4-2B. 1500 cells/well were seed. Data was acquired at 14 days after seeding. Total colony area was measured using Image-J. Experiments were repeated 3 times. (d) Effects of TAZ knockdown on tumor spheroid formation of C4-2B. 500 cells were suspended in 50ul of matrigel and seed in each well of 24 wells ultra-low binding plates. Numbers of tumor spheroids (>50um) were counted after 14 day culture. Scale bar = 200um. Experiment was independently repeated 3 times.

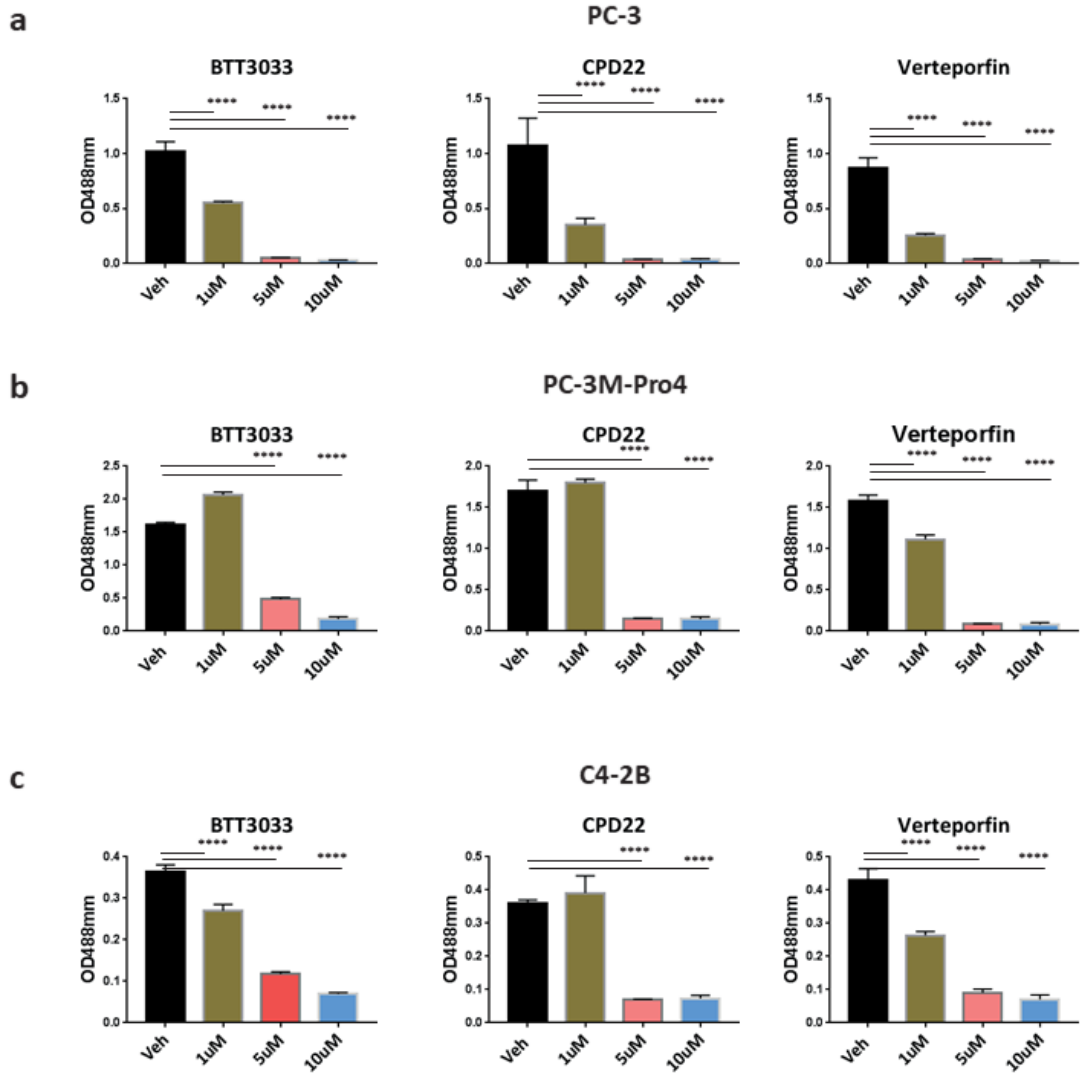

Fig. S7 Chemical inhibition of integrin-β1, ILK and YAP/TAZ suppresses PCa cell growth. PC-3 (a), PC-3M-Pro4 (b) and C4-2B (c) were respectively treated with integrin-β1 inhibitor BTT3033, ILK inhibitor CPD22 and YAP/TAZ inhibitor Verteporfin for 72 hours. Cell viability was measured using WST reagent. Each experiment was repeated 3 times.